

# **Influence of Molecular Hydrogen on Bulk and Interfacial Properties of Three Imidazolium-Based Ionic Liquids by Experiments and Molecular Dynamics Simulations**

*Ziwen Zhai<sup>1+</sup>, György Hantal<sup>2+</sup>, Arsha Cherian<sup>2</sup>, Alexander Bergen<sup>3</sup>, Junyu Chu<sup>3</sup>, Christian R. Wick<sup>2</sup>, Karsten Meyer<sup>3</sup>, Ana-Sunčana Smith<sup>2</sup>, Thomas M. Koller<sup>1\*</sup>*

<sup>1</sup>Institute of Advanced Optical Technologies – Thermophysical Properties (AOT-TP), Department of Chemical and Biological Engineering (CBI) and Erlangen Graduate School in Advanced Optical Technologies (SAOT), Friedrich-Alexander-Universität Erlangen-Nürnberg (FAU), Paul-Gordan-Straße 8, 91052 Erlangen, Germany

<sup>2</sup>PULS Group, Department of Physics, Interdisciplinary Center for Nanostructured Films, Friedrich-Alexander-Universität Erlangen-Nürnberg (FAU), 91058 Erlangen, Germany

<sup>3</sup>Department of Chemistry and Pharmacy, Inorganic Chemistry, Friedrich-Alexander-Universität Erlangen-Nürnberg (FAU), Egerlandstraße 1, 91058 Erlangen, Germany

---

\*Author to whom correspondence should be addressed: email: [thomas.m.koller@fau.de](mailto:thomas.m.koller@fau.de), ORCID number 0000-0003-4917-3079.

<sup>+</sup>Shared first-authorship due to equal contributions

## ABSTRACT

Despite the presence of molecular hydrogen (H<sub>2</sub>) in various technical applications involving ionic liquids (ILs), its effect on the bulk and interfacial properties of ILs is poorly understood. The present study investigates the influence of dissolved H<sub>2</sub> on the viscosity, surface tension, and phase composition of three imidazolium-based ILs by experiments and Molecular Dynamics (MD) simulations between (303 and 393) K from (0.1 to 31) MPa. The surface light scattering and pendant-drop experiments showed for all three ILs that the saturated liquid viscosity does not significantly change with increasing H<sub>2</sub> pressure, while the surface tension decreases about 5% at 8 MPa. The MD simulations could be used to clarify microscopic origins for the behavior of the macroscopic properties. They revealed not only a compensation of compression and solvation effects due to hydrostatic pressure and dissolved H<sub>2</sub> on the viscosity, but also a weak enrichment of H<sub>2</sub> at the IL-gas interfaces.

**KEYWORDS** – experiments, hydrogen, ionic liquids, Molecular Dynamics simulations, surface tension, viscosity

## ABBREVIATIONS

Ar	argon
[C <sub>2</sub> C <sub>1</sub> Im][NTf <sub>2</sub> ]	1-ethyl-3-methylimidazolium bis(trifluoromethanesulfonyl)imide
[C <sub>8</sub> C <sub>1</sub> Im][PF <sub>6</sub> ]	1-methyl-3-octylimidazolium hexafluorophosphate
CF	correlation function
CO <sub>2</sub>	carbon dioxide
FF	force field
H <sub>2</sub>	hydrogen
IFF	Interface Force Field
IL	ionic liquid
ITIM	Identification of Truly Interfacial Molecules
LOHC	liquid organic hydrogen carriers
MD	Molecular Dynamics

[(mPEG <sub>2</sub> ) <sub>2</sub> Im] I	1,3- <i>bis</i> (2-(2-ethoxyethoxy)ethyl)imidazolium iodide
N <sub>2</sub>	nitrogen
PD	pendant drop
PME	Particle-Mesh Ewald
SASA	solvent-accessible surface area
SILP	Supported Ionic Liquid Phase
SLS	surface light scattering
YL	Young-Laplace

## Introduction

Ionic liquids (ILs) are molten salts of diverse combinations of anions and cations that have attracted considerable attention as tailor-made fluids due to their melting temperatures below 100°C and low vapor pressures [1]. These and other special characteristics have rendered ILs as interesting working fluids for a wide range of technical applications in both research and industry [1–5]. For example, ILs can be used as electrolytes [1,6], media for heat transfer and energy storage [7,8] or for gas separation [9,10] as well as solvents for catalysis in Supported Ionic Liquid Phase (SILP) systems [11]. SILP materials involve homogeneous catalysts in the form of metal complexes dispersed in thin IL films coated on solid supports [12–15]. This concept combines the high selectivity and activity of homogeneous catalysis with the ease of product separation provided by heterogeneous catalysis. Nowadays, SILP systems are considered in important industrial applications involving molecular hydrogen (H<sub>2</sub>), including hydrogenation and dehydrogenation reactions relevant for hydrogen storage [16], hydroformylation [15,17–20], hydrodesulfurization [21–23], and syngas reactions [24,25]. In all these cases, H<sub>2</sub> as the lightest molecular species partially dissolves in the SILP film, while the rest builds a gas phase above the IL-rich phase.

For the design and performance of the aforementioned catalytic technologies, knowledge of the thermophysical properties of ILs in the presence of H<sub>2</sub> is of key importance. In the present study, we focus on the liquid dynamic viscosity  $\eta_L$  and the surface tension  $\sigma$  as characteristic macroscopic bulk and interfacial properties of IL films, respectively. These two properties govern processes and mechanisms in SILP systems, particularly in those designed for Interface-enhanced catalysis preferentially at the gas-liquid interface [26] relevant for this work, and/or at the solid-liquid interface [27,28]. For example, surface tension controls the mass transfer of H<sub>2</sub> across the gas-liquid interface and the wetting on the support [19,20]. The viscosity has a significant influence on the diffusive mass transport of reactants, products, and dissolved metal catalysts within the SILP film [29,30]. Possible changes induced by H<sub>2</sub> on the surface tension and viscosity of ILs at process-relevant pressure  $p$  and temperature  $T$  conditions may subsequently influence mass and momentum transport as well as the reaction kinetics, ultimately impacting the overall SILP efficiency.

There have been a few experimental studies on the influence of H<sub>2</sub> on  $\sigma$  and  $\eta_L$  of non-electrolytic liquids, including linear or branched alkanes [31–34], alcohols [31,34,35], or hydrocarbon-based liquid organic hydrogen carriers [36]. For all these solvent types, only minor changes in both properties compared to the values of the pure fluids could be found for H<sub>2</sub> pressures up to about 8 MPa. While the viscosity was found to be unaffected by the presence

of H<sub>2</sub>, a slight decrease in the surface tension with increasing H<sub>2</sub> pressure in the order of about 5% at 8 MPa could be observed. Such behavior is strongly related to the relatively low solubility of H<sub>2</sub>, which is the property that has received the most attention [37–39] as recently reviewed by Lei et al. [40]. Notably, however, certain inconsistencies in the solubility data sets were found and attributed to challenges in accurately measuring the solubilities of a poorly soluble gas like H<sub>2</sub> in ILs [37,38,41–43]. Metrological challenges are further enhanced for studying  $\sigma$  and  $\eta_L$  of mixtures of ILs and H<sub>2</sub> at equilibrium conditions when the measurements need to be performed at or very close to saturation. This is often not guaranteed, or even possible, in classical tensiometry and viscometry. This experimental complexity may explain why corresponding investigations for IL-H<sub>2</sub> mixtures have not been conducted until today.

A complementary approach to understand the physical and chemical properties of IL systems are molecular dynamics (MD) simulations. Because they provide atomic resolution, MD simulations can also be used to elucidate the molecular mechanisms underlying given effects including solubility or interface composition. Therefore, the first simulation studies of ILs and the first related general-purpose force fields (FF) appeared as early as the interest in the application of ILs has grown 25 years ago. IL interfaces soon attracted considerable interest too: Lynden-Bell was the first to report on the preferential orientation of cations and the resulting accumulation of alkyl groups at the vapor-liquid interface of alkyimidazolium-based ILs [44]. A decade later, the first intrinsic surface analyses were also performed on vapor-liquid and liquid-liquid interfaces containing ILs [45,46]. Later, additional interface analysis tools were developed in order to reveal the change in surface composition as a function of the length of the cation's side chain [30,47]. MD studies were also used to study the solubility of small gases in ILs. One such study revealed the molecular mechanism of competitive gas adsorption in supported IL films relevant for gas separation [48]. In this study, the focus was on the adsorption and the absorption of an equimolar carbon dioxide (CO<sub>2</sub>)-nitrogen (N<sub>2</sub>) mixture in an IL film, whereby the dependence of the selectivity of the IL layer on the thickness of the film could be rationalized. The solubility and solvation free energy of light gases in imidazolium-based ILs of varying cation side chain length was also explored [49]. For H<sub>2</sub>, its solubility was studied in one particular IL and was found to increase with increasing temperature [50]. However, a deepened understanding on the influence of H<sub>2</sub> on the macroscopic and microscopic properties of ILs remains by end large unexplored to this date.

The present study aims to rectify this situation and to resolve the influence of H<sub>2</sub> on the bulk and interfacial properties of three imidazolium-based ILs by experiments and MD simulations. This study continues our previous research on investigating experimentally the

effects of gases such as CO<sub>2</sub> and argon (Ar) on the thermophysical properties of ILs [51,52], and on modeling the bulk and interfacial properties of ILs [30,45,46,53]. In line with these investigations, the model ILs selected in the present work are the hydrophobic 1-ethyl-3-methylimidazolium bis(trifluoromethanesulfonyl)imide ([C<sub>2</sub>C<sub>1</sub>Im][NTf<sub>2</sub>]) and 1-methyl-3-octylimidazolium hexafluorophosphate ([C<sub>8</sub>C<sub>1</sub>Im][PF<sub>6</sub>]) as well as the hydrophilic 1,3-*bis*(2-(2-ethoxyethoxy)ethyl)imidazolium iodide ([mPEG<sub>2</sub>]<sub>2</sub>Im]I), which also make it possible to cover a wide range of values of viscosities and surface tensions. The measurements on  $\eta_L$  and  $\sigma$  were performed using surface light scattering (SLS) and the pendant-drop (PD) method in the temperature range from (303 to 353) K and H<sub>2</sub> pressures range from (0.1 to 8) MPa. The simulations were conducted at equivalent conditions, providing same trends as observed in the experiments. Additional valuable information on the density and composition of the liquid phase and, in particular, on the fluid structure of the gas-liquid interface are also provided by the simulations. This synergistic approach allows us to explain the origins for the changes in viscosity and surface tension induced by pressurized H<sub>2</sub>.

## Experiments and Molecular Dynamics (MD) Simulations

### *Materials and sample preparation*

The specifications of the three ILs and the hydrogen (H<sub>2</sub>) gas studied in this work are listed in Table 1. The two ILs [C<sub>2</sub>C<sub>1</sub>Im][NTf<sub>2</sub>] and [C<sub>8</sub>C<sub>1</sub>Im][PF<sub>6</sub>] as well as H<sub>2</sub> were obtained commercially by suppliers. A sample of the IL ([mPEG<sub>2</sub>]<sub>2</sub>Im]I) was self-synthesized according to a procedure described by Seidl et al. [47]. Prior to the SLS and PD measurements, the optical quality of all three IL samples was checked by irradiation of laser light, showing no noteworthy presence of larger particles. In addition, potential volatile impurities such as water and dissolved air were removed from the IL through additional evacuation, as outlined in our previous study [52]. Thereafter, the water content of the ILs was determined by Karl–Fischer coulometric titration consecutively, with the filling procedure under Ar atmosphere, after which the entire manifold was degassed before gas addition for each system.

**Table 1** – Specifications of the studied samples.

substance	CAS number	source	molar mass <i>M</i> / (g·mol <sup>-1</sup> )	purity <sup>a</sup>	water content <sup>c</sup> / ppm
ethyl-3-methylimidazolium bis(trifluoromethylsulfonyl) imide ([C <sub>2</sub> C <sub>1</sub> Im][NTf <sub>2</sub> ])	174899-82-2	IoLiTec	391.30	$w \geq 0.995$	108.9
1-methyl-3-octylimidazolium hexafluorophosphate ([C <sub>8</sub> C <sub>1</sub> Im][PF <sub>6</sub> ])	304680-36-2	IoLiTec	340.29	$w \geq 0.99$	100.4

1,3-bis(2-(2-ethoxyethoxy)ethyl)imidazolium iodide ([(mPEG) <sub>2</sub> Im]I)	-	self-made	400.26	N/A <sup>b</sup>	1009.4
hydrogen (H <sub>2</sub> )	1333-74-0	Linde AG	2.0159	$\varphi \geq$ 0.999999 <sup>b</sup>	-

<sup>a</sup> Purity in the form of weight fraction  $w$  or volume fraction  $\varphi$  as specified by the supplier.

<sup>b</sup> Synthesized and purified according to literature [47].

<sup>c</sup> Value determined by Karl–Fischer coulometric titration before the experiments with an estimated relative expanded (coverage factor  $k = 2$ ) uncertainty of less than 20%.

### ***Experimental procedure and data evaluation***

The influence of H<sub>2</sub> on the thermophysical properties  $\sigma$  and  $\eta_L$  was examined using a combined SLS-PD setup. This setup is identical to the one utilized in our previous works on pure ILs [54,55] and binary IL mixtures [51,52]. Details of the setup including the used measurement cell can be found in Refs. [52,54]. The following thermodynamic states were adjusted in the measurements by the PD method and SLS: In total, a  $T$  range from (303.15 to 353.15) K and a H<sub>2</sub>  $p$  range from (0.1 to 8.0) MPa were covered. At 303.15 K, a finer H<sub>2</sub> pressure variation with  $p$  states of (0.1, 2.0, 4.0, 6.0, and 8.0) MPa was used for all three ILs. The same  $p$  states were also studied in connection with the PD measurements on [(mPEG)<sub>2</sub>Im]I + H<sub>2</sub> at 353 K. For all other systems studied at (323 and 353) K, the H<sub>2</sub> pressures were limited to three values of (0.1, 4.0, and 8.0) MPa. Prior to the measurements with H<sub>2</sub>, reference measurements were conducted for all three ILs at 303.15 K with 0.1 MPa Ar. This allowed us to ensure the verify the results for  $\sigma$  and  $\eta_L$  of the practically pure ILs against data from our previous studies [51,54,55].

The temperature control of the SLS/PD-measurement cell and the sample vessel used as a reservoir for the PD experiments was realized by resistant heating and Pt-100  $\Omega$  probes with expanded (coverage factor  $k = 2$ ) uncertainties of 0.02 K. The reported  $T$  was recorded by a probe placed next to the PD inside the measurement sample cell with a stability better than  $\pm 0.05$  K. The pressures within the measurement cell and a connected sample vessel were continually monitored using pressure transmitters featuring an expanded uncertainty ( $k = 2$ ) of 5 kPa. The reported values for  $p$  are the average values obtained during the SLS measurements with a stability of  $\pm 5$  kPa. For the accurate determination of surface tension  $\sigma$  and viscosity  $\eta_L$  at macroscopic thermodynamic equilibrium, PD and SLS experiments were performed consecutively once both  $T$  and  $p$  remained constant.

#### ***Pendant-drop (PD) method – surface tension***

To determine the gas-liquid surface tension of the binary mixtures of IL with H<sub>2</sub>, the PD method has been employed. Here, the shape of an axisymmetric PD hanging on a capillary and exposed

to the gravitational field is governed by the competition between gravitational, buoyancy, and capillary forces. The working principle of the PD method is based on the comparison of the experimentally obtained drop contour with the theoretically calculated drop profile. The latter profile is defined by the Young-Laplace (YL) equation for curved interfaces [56]. In each measurement series, an IL sample stored in the sample vessel was pre-heated to the same temperature as the measurement cell, but pre-saturated with gas at a slightly higher pressure which was approximately 0.01 MPa larger than inside the cell. This allowed to generate PDs within the sample cell by liquid transfer. For each thermodynamic state, a defined procedure was carried out, which involves the calibration of the optical system and the droplet formation and recording for various droplets, as it is detailed in our previous work [52]. Subsequently, the PD images were analyzed with a self-written evaluation code [57] based on the axisymmetric drop shape analysis [58].

For solving the YL equation, the liquid density  $\rho_L$  and gas density  $\rho_G$  are needed. These values were employed from literature, as detailed in section S1 of the Supporting Information. Since the solubility of H<sub>2</sub> in the studied ILs is relatively small up to elevated  $p$  of 8 MPa, as discussed later in the section “Results and Discussion – H<sub>2</sub> solubility in ILs,”  $\rho_L$  of the binary IL-H<sub>2</sub> mixtures can be reliably approximated with that of the pure ILs at 0.1 MPa. This is also justified by our MD simulation results for the liquid density of the binary IL-H<sub>2</sub> mixtures up to high  $p$ , which does not significantly deviate from the values of the pure ILs at 0.1 MPa (see Table S2 in Supporting Information). The final reported data for  $\sigma$  are obtained by averaging the results from in total 25 images per state point. The expanded (coverage factor  $k = 2$ ) uncertainty of 2% for  $\sigma$  accounts for the uncertainties originating from the calibration procedure and the input parameters.

#### *Surface light scattering (SLS) – viscosity and surface tension*

At the same states as studied by the PD method, SLS has been utilized for the determination of the saturated liquid viscosity  $\eta_L$  and, in a few cases, also the gas-liquid surface tension  $\sigma$  of the IL-H<sub>2</sub> mixtures. The method relies on analyzing the dynamics of surface fluctuations present at the gas-liquid interface in macroscopic thermodynamic equilibrium. For a detailed description of the theory behind SLS [59–61] and its application in thermophysical property research of different working fluids [62,63] including ILs [52,54], the reader is referred to the given references. In the following, only the information essential for this work is summarized.

Considering the opaque color of some IL samples, SLS measurements were performed in reflection direction. Here, using coherent laser light with a wavelength of 532 nm in vacuo

at a sufficiently small incident laser power, the light scattered by the gas-liquid interface was detected perpendicularly to the interface near the reflected beam. To realize a heterodyne detection scheme, a frequency-unshifted reference light of much larger intensity was added to the scattered light. For each state, four individual SLS measurements corresponding to a defined wave vector  $q$  of the studied surface fluctuations between (4.12 and 5.44)  $\text{m}^{-1}$  were conducted. The light scattering signals were recorded by two Avalanche photodiodes and processed via a single- $\tau$  correlator to determine the second-order pseudo-cross correlation functions (CFs) of the scattered light intensity  $g^{(2)}(\tau)$  as a function of the delay time  $\tau$ .

Depending on the reduced capillary number  $Y$ , two different cases for the temporal behavior of surface fluctuations were observed, which are also exemplarily illustrated in Fig. 1 for SLS experiments on a mixture of  $[\text{C}_2\text{C}_1\text{Im}][\text{NTf}_2]$  with  $\text{H}_2$  at a pressure of 8.0 MPa at 303.15 K (a) and 353.14 K (b). For the majority of measurements, an overdamped behavior ( $Y < 0.145$ ) was found, which corresponds to a scenario for fluids with a relatively large  $\eta_{\text{L}}$ . As shown in Fig. 1a, the exponentially decaying CF can be characterized by their decay time  $\tau_{\text{C}}$  with a typical expanded ( $k = 2$ ) fit uncertainty of approximately 2%. The uncertainties in  $\tau_{\text{C}}$  increase up to about 6% near the critical damping ( $Y \approx 0.145$ ). Only for the system  $[\text{C}_2\text{C}_1\text{Im}][\text{NTf}_2] + \text{H}_2$  at 353 K, an oscillatory behavior of surface fluctuations ( $Y > 0.145$ ) was observed, where the fluids show a relatively small  $\eta_{\text{L}}$ . Here, the CFs reflect damped oscillations which are described by their decay time  $\tau_{\text{C}}$  and the frequency  $\omega_{\text{q}}$ . This can be seen in Fig. 1b, yielding typical fit uncertainties ( $k = 2$ ) of 3% for both  $\tau_{\text{C}}$  and  $\omega_{\text{q}}$ . The residual plots in the lower part of Fig. 1 are free of any systematics, demonstrating that the experiments agree with theory.

For an accurate determination of  $\eta_{\text{L}}$  in the overdamped case or both  $\eta_{\text{L}}$  and  $\sigma$  in the oscillatory case, the dispersion relation for the dynamics of hydrodynamic surface fluctuations [59,60] was used in its complete form. For this, besides  $\tau_{\text{C}}$  and  $\omega_{\text{q}}$  further thermophysical parameters are required as an input.  $\rho_{\text{G}}$  and  $\rho_{\text{L}}$  are taken from the same sources as used for the PD evaluation. Furthermore, the dynamic viscosity of the gas phase containing solely  $\text{H}_2$  was employed from literature, see section S1 and Table S1 in the Supporting Information. In the overdamped case, the data for  $\sigma$  from the PD method are additionally used to obtain  $\eta_{\text{L}}$ . The final results are the unweighted averages from the four different individual measurements at different  $q$ . For the expanded ( $k = 2$ ) uncertainties, values between (2 and 7)% for  $\eta_{\text{L}}$  and between (1 and 5)% for  $\sigma$  were determined from error propagation calculations. The larger uncertainties are related to the complexity of evaluating SLS signals near the critical damping.

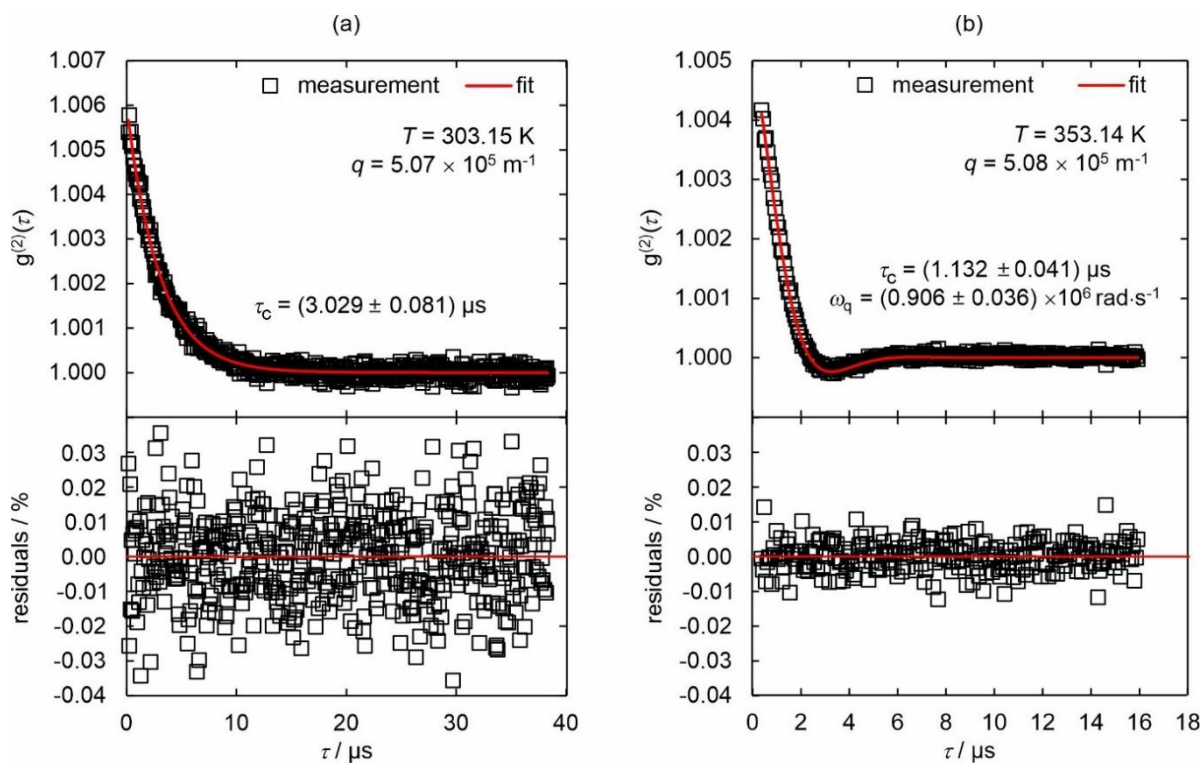


**Fig. 1** – Example normalized CFs (upper part) and their residuals from the corresponding fits (lower part) as a function of delay time  $\tau$  obtained from SLS experiments on mixtures of  $[\text{C}_2\text{C}_1\text{Im}][\text{NTf}_2]$  with dissolved  $\text{H}_2$  at  $p = 8.0$  MPa for  $T = 303.15$  K (a) and  $353.14$  K (b). (designed for double-column image)

### *Molecular Dynamics (MD) simulations*

#### *Force field parameters and simulation details*

Non-polarizable all-atom force fields (FFs) were applied for the MD simulations of the studied ILs and  $\text{H}_2$ . All FFs account for intramolecular and intermolecular interactions, where the latter are represented by pairwise electrostatic and van der Waals interactions through the Coulombic and Lennard–Jones 12-6 potential, respectively.  $[\text{C}_2\text{C}_1\text{Im}][\text{NTf}_2]$  was described by the FF developed by Maginn et al. [64] with partial charges adjusted to optimize by refitting the partial atomic charges on a larger set of conformations [53]. To simulate  $[(\text{mPEG}_2)_2\text{Im}]\text{I}$ , the FF parameters for the cation proposed in the work of Seidl et al. [47] were further optimized to account for the flexibilities of the side chains (see section S2 in the Supporting Information for the new charge set). Molecular  $\text{H}_2$  was modeled with the Interface Force Field (IFF) which was shown to be compatible with commonly used FFs such as AMBER [65].

All MD simulations were performed with the GROMACS 2022.4 program package using three-dimensional periodic boundary conditions. The integration time step for the equations of motions was set to 2 fs for pure ILs and to 1 fs for IL systems with dissolved  $\text{H}_2$ . Non-bonded interactions were cut off at 1.2 nm, and the long-range part of the electrostatic interactions was accounted for by using the Particle-Mesh Ewald (PME) method. Van der

Waals interactions were shifted such that they were 0 at the cut-off distance. MD simulations were performed on a single-phase liquid or a two-phase gas-liquid system, as described below.

### *Viscosity calculations*

As stated above, the shear viscosity  $\eta_L$  of the ILs was modeled in the single-phase liquid state. For this, the Green-Kubo method analyzing the autocorrelation function of the off-diagonal elements of the pressure tensor at equilibrium conditions is often employed [66,67]. Since such viscosity calculations are known to be challenging due to convergence issues (worsening with increasing  $\eta_L$ ) [64], an alternative non-equilibrium approach was used in this work and only applied to [C<sub>2</sub>C<sub>1</sub>Im][NTf<sub>2</sub>] because of its low viscosity. This approach is the so-called periodic perturbation method [68], which is based on the application of a position-dependent periodic acceleration on the system and the subsequent computation of the resulting velocity field in response to the stimulus. The viscosity is determined from the maximum amplitude of the computed periodic velocity profile and the maximum amplitude of the acceleration applied to the system. The latter needs to be carefully set within an optimum value range determined by the necessity of a resulting static velocity profile, while the liquid should still display a Newtonian behavior. These conditions translate into the requirements of both a low fitting error of the velocity profile and the insensitivity of the viscosities on the maximum shear rate.

To determine the viscosity, a homogenous bulk phase containing 750 ion pairs was used. In one series, pure [C<sub>2</sub>C<sub>1</sub>Im][NTf<sub>2</sub>] was studied by imposing an isotropic pressure of (0.1, 4, or 8) MPa at (298, 323, or 353) K. In a second series, the simulations were carried out the same temperatures and an applied pressure of 8 MPa, containing this time dissolved H<sub>2</sub> corresponding to the saturated solutions at the given conditions. The comparison of the computed values from the two series allows to separate the effects resulting solely from the hydrostatic pressure itself and from the impact of H<sub>2</sub>. In order to determine the optimum range of maximum acceleration amplitudes, all viscosity calculations were repeated three times at roughly 12-20 acceleration values in every state point. All simulations lasted for 20 ns out of which only the last 15 ns was used to evaluate the viscosity. For every average value, a sample of 15-20 points was used, each with an associated fitting error. Cumulated uncertainties ( $k = 1$ ) were determined at every state point as standard errors of the sample through error propagation formulas.

### *Surface tension calculations*

The surface tension  $\sigma$  was computed at different state points in a two-phase gas-liquid system involving an interface in the *NVT* ensemble. These interface systems contained an IL slab of

700 ion pairs saturated with H<sub>2</sub> in equilibrium with a pure H<sub>2</sub> phase. [C<sub>2</sub>C<sub>1</sub>Im][NTf<sub>2</sub>] was studied at (298, 323 and 353) K containing 0, 1,500, 3,000, 5,000, or 10,000 H<sub>2</sub> molecules. Since [(mPEG<sub>2</sub>)<sub>2</sub>Im]I turned out to be very viscous, it was studied only at (353 and 393) K, with 0, 3,000, or 10,000 H<sub>2</sub> molecules added to the IL in the simulation box. A very careful equilibration procedure was followed to ensure that the systems reach equilibrium compositions in all conditions: At a given state point, the required number of H<sub>2</sub> molecules was inserted entirely in either the vacuum or the IL phase, and two separate equilibrations were carried out for each system until the same composition was reached. Accordingly, equilibration simulations lasted between (800 and 3,000) ns, depending on the system (more details on the system preparation can be found in section S3 of the Supporting Information). Subsequently, 400-2,000 ns equilibrium trajectories were used to compute the equilibrium pressure, liquid phase compositions, and the surface tension. The mole fraction of H<sub>2</sub> in the liquid phase,  $x_{\text{H}_2}$ , was characterized through partial density profiles computed along the  $z$ -coordinate of the simulation box across the interface.  $\sigma$  was calculated from the difference of the lateral and normal components of the pressure tensor according to the mechanical (or virial) route as implemented in Gromacs [53,67]. Uncertainties of the final values for  $\sigma$  and  $x_{\text{H}_2}$ , were determined as standard errors ( $k = 1$ ) through block averaging by splitting the equilibrium trajectories into 5-6 blocks. A snapshot of a typical simulation box for the two-phase gas-liquid system containing [C<sub>2</sub>C<sub>1</sub>Im][NTf<sub>2</sub>] and H<sub>2</sub> at 8 MPa and 323 K can be seen in Fig. 2, where the liquid IL-H<sub>2</sub> phase in the middle is surrounded by a H<sub>2</sub> gas phase on both sides, resulting in two interfaces.

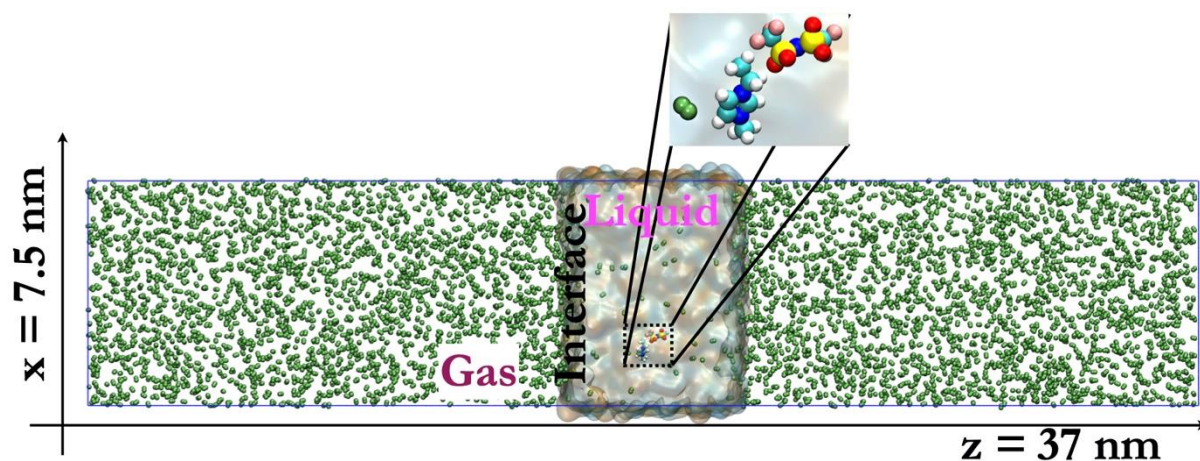


**Fig. 2** – 2D-Projection of a 3D simulation box of a gas-liquid system consisting of an [C<sub>2</sub>C<sub>1</sub>Im][NTf<sub>2</sub>]-H<sub>2</sub> liquid film and a H<sub>2</sub> gas phase at 323 K and 8 MPa. The H<sub>2</sub> molecules are indicated by green color. (designed for double-column image)

## Results and Discussion

The experimental and MD simulation results will be discussed in this chapter, starting with a data summary of the relevant thermophysical properties of interest. Thereafter, two macroscopic bulk properties of the liquid phase, namely the H<sub>2</sub> solubility and the viscosity, are discussed. Finally, the last section delves into gas-liquid interfacial properties, focusing on the macroscopic surface tension and the microscopic surface structure. In these latter two sections, the experimental data for  $\eta$  and  $\sigma$  will be presented and discussed first, before they are compared with the simulation results. The latter will also be used to interpret the experimental findings.

### *Summary of thermophysical property values from experiments and MD simulations*

For the binary mixtures of three studied ILs [(mPEG<sub>2</sub>)<sub>2</sub>Im]I, [C<sub>8</sub>C<sub>1</sub>Im][PF<sub>6</sub>], or [C<sub>2</sub>C<sub>1</sub>Im][NTf<sub>2</sub>] with dissolved H<sub>2</sub>, the experimental results for  $\eta_L$  accessed via SLS as well as the  $\sigma$  obtained by both PD method and, in parts, also by SLS are summarized in Table 2 together with their expanded ( $k = 2$ ) uncertainties. The pressure and temperature ranges covered in the experiments are between about (0.1 to 8.0) MPa and (303 to 353) K. The corresponding input parameters used for the evaluation of the SLS and PD experiments, i.e.  $\rho_L$ ,  $\rho_G$ , and  $\eta_G$ , are provided in Table S1 in the Supporting Information. The  $T$ - and  $p$ -dependent MD simulation results from the single-phase simulations on [C<sub>2</sub>C<sub>1</sub>Im][NTf<sub>2</sub>] without or with H<sub>2</sub> and from the two-phase simulations on [(mPEG<sub>2</sub>)<sub>2</sub>Im]I or [C<sub>2</sub>C<sub>1</sub>Im][NTf<sub>2</sub>] without or with H<sub>2</sub> can be found in section S4 of the Supporting Information, respectively. Here, Table S2 includes not only the surface tension  $\sigma$ , but also the partial densities of the IL ( $\rho_{L,IL}$ ) and H<sub>2</sub> ( $\rho_{L,H_2}$ ) as well as the H<sub>2</sub> mole fraction  $x_{H_2}$  in the liquid phase. Furthermore, Table S3 lists the results for  $\eta_L$ .

**Table 2** - Surface tension  $\sigma$  and liquid dynamic viscosity  $\eta_L$  of binary mixtures of [(mPEG<sub>2</sub>)<sub>2</sub>Im]I, [C<sub>8</sub>C<sub>1</sub>Im][PF<sub>6</sub>], or [C<sub>2</sub>C<sub>1</sub>Im][NTf<sub>2</sub>] with dissolved H<sub>2</sub> including percentage expanded ( $k = 2$ ) uncertainties  $U_r$  obtained by the PD method (index “PD”) and SLS (index “SLS”) at macroscopic thermodynamic equilibrium as a function of pressure  $p$  at different temperatures  $T$ . For the data evaluation, the required input data for the liquid density  $\rho_L$ , gas density  $\rho_G$ , and gas viscosity  $\eta_G$  are provided in section S1 of the Supporting Information.

$T / K$	$p / \text{MPa}$	$\sigma^{\text{PD}} / (\text{mN}\cdot\text{m}^{-1})$	$100\cdot U_r(\sigma^{\text{PD}})$	$\sigma^{\text{SLS}} / (\text{mN}\cdot\text{m}^{-1})$	$100\cdot U_r(\sigma^{\text{SLS}})$	$\eta_L / (\text{mPa}\cdot\text{s})$	$100\cdot U_r(\eta_L)$
[(mPEG <sub>2</sub> ) <sub>2</sub> Im]I + H <sub>2</sub>							
303.16	0.12	45.33	2	-	-	568.3	2.5
303.17	2.00	44.85	2	-	-	582.5	3.6
303.15	4.00	44.43	2	-	-	582.9	2.8
303.17	6.00	43.97	2	-	-	595.0	3.2

303.17	8.01	43.47	2	-	-	599.1	3.1
323.14	0.11	44.00	2	-	-	151.6	4.4
323.15	4.00	42.99	2	-	-	152.4	6.6
323.14	8.00	42.15	2	-	-	156.2	4.3
353.15	0.11	42.06	2	-	-	-	-
353.14	1.00	41.71	2	-	-	-	-
353.14	2.00	41.41	2	-	-	-	-
353.15	4.00	41.12	2	-	-	-	-
353.13	6.00	40.78	2	-	-	-	-
353.15	8.00	40.46	2	-	-	-	-
[C <sub>8</sub> C <sub>1</sub> Im][PF <sub>6</sub> ] + H <sub>2</sub>							
303.14	0.11	34.01	2	-	-	516.3	2.1
303.15	2.00	33.67	2	-	-	522.8	2.4
303.14	4.00	33.13	2	-	-	520.2	2.1
303.14	6.05	32.77	2	-	-	524.3	2.1
303.14	8.00	32.15	2	-	-	523.2	2.2
323.14	0.12	32.86	2	-	-	159.1	2.2
323.13	4.04	32.06	2	-	-	159.2	2.4
323.14	8.00	31.22	2	-	-	156.2	2.4
[C <sub>2</sub> C <sub>1</sub> Im][NTf <sub>2</sub> ] + H <sub>2</sub>							
303.15	0.10	35.84	2	-	-	27.00	2.8
303.15	1.99	35.42	2	-	-	27.16	3.0
303.15	4.00	35.09	2	-	-	27.21	2.8
303.15	6.01	34.66	2	-	-	27.37	2.8
303.15	8.01	34.36	2	-	-	27.59	3.2
323.16	0.11	34.81	2	-	-	15.51	5.2
323.15	4.00	34.13	2	-	-	15.73	5.8
323.20	8.01	33.45	2	-	-	-	-
353.14	0.10	33.27	2	34.18	1.1	7.580	3.3
353.16	3.99	32.74	2	33.27	2.8	7.637	3.9
353.14	8.02	32.08	2	32.82	4.6	7.762	4.3

### ***Bulk properties***

#### *H<sub>2</sub> solubility in ILs*

Due to the very low solubility of H<sub>2</sub> in the studied ILs, it was not possible to derive quantitative values for  $x_{\text{H}_2}$  based on the gas-adsorption technique within our combined PD/SLS-setup. Therefore, MD simulations on the two-phase IL-H<sub>2</sub> systems could be used to estimate  $x_{\text{H}_2}$  in [C<sub>2</sub>C<sub>1</sub>Im][NTf<sub>2</sub>] and [(mPEG<sub>2</sub>)<sub>2</sub>Im]I for  $T$  between (298 and 393) K and  $p$  up to 31 MPa, as summarized in Table S2. These results are displayed in Fig. 3, where the common representation of  $p$  shown as a function of  $x_{\text{H}_2}$  is used.

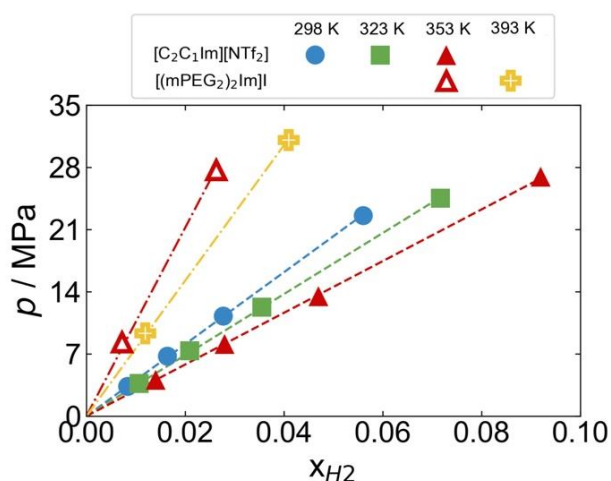


**Fig. 3** – Computed values for solubility of H<sub>2</sub> in [C<sub>2</sub>C<sub>1</sub>Im][NTf<sub>2</sub>] (full symbols) and [(mPEG<sub>2</sub>)<sub>2</sub>Im]I (empty symbols) as a function of pressure for different temperatures obtained from MD simulations. The dashed ([C<sub>2</sub>C<sub>1</sub>Im][NTf<sub>2</sub>]) and dash-dotted ([[(mPEG<sub>2</sub>)<sub>2</sub>Im]I]) lines represent linear fits to the data sets by additionally imposing the fit through the origin in order to estimate the Henry’s law constants shown in Table 3. (designed for single-column image)

Both studied ILs show very low H<sub>2</sub> solubilities, with maximum values of  $x_{H_2} = 0.092$  for [C<sub>2</sub>C<sub>1</sub>Im][NTf<sub>2</sub>] at 27 MPa and 353 K as well as  $x_{H_2} = 0.041$  at 31 MPa and 393 K for the studied conditions. The comparison of the solubilities in the different ILs at the same temperature of 353 K reveals an about 3.5 higher solubility in the hydrophobic [C<sub>2</sub>C<sub>1</sub>Im][NTf<sub>2</sub>] compared to the hydrophilic [(mPEG<sub>2</sub>)<sub>2</sub>Im]I. This behavior seems to be related to the non-polar nature of H<sub>2</sub>, which causes its dissolution in a hydrophobic IL to be more favorable. For all  $T$  and both ILs,  $p$  increases linearly with increasing  $x_{H_2}$ , which allows us to apply a linear fit to each individual data set with the constraint of passing through the origin, see Fig. 3. The slopes of the fitted lines serve as estimates for Henry’s law constants,  $H_{H_2} = p/x_{H_2}$ , which are displayed in Table 3 for a particular IL at a given  $T$ . The observed decrease of the estimated Henry’s law constants with increasing  $T$  comes along with an increasing H<sub>2</sub> solubility, which is characteristic of gases with endothermic solvation enthalpies. The qualitative behavior of the present MD results for  $x_{H_2}$  with respect to the influence of  $p$ ,  $T$ , and IL characteristics agrees with the conclusions drawn in the review article of Lei et al. [40] and, in particular, with the experimental results for the H<sub>2</sub> solubility in [C<sub>*n*</sub>C<sub>1</sub>Im][NTf<sub>2</sub>] IL ( $n = 2, 4, 6$ ) including [C<sub>2</sub>C<sub>1</sub>Im][NTf<sub>2</sub>]. For the latter IL, the measured high-pressure values for  $x_{H_2}$  determined by Raeissi et al. [39] are in sound agreement with the predictions from our MD simulations at comparable  $p$  and  $T$ . For example, the experimental value  $x_{H_2} = 0.0559$  at 12.45 MPa and 351.6 K is close to the modeled value  $x_{H_2} = 0.047$  at 13.45 MPa and 353.15 K. A quantitative data comparison with the experimental H<sub>2</sub> solubilities reported by Doblinger et al. [37] and Jacquemin et al. [38] is hardly possible due to the very small H<sub>2</sub> pressures of only up to about 0.1 MPa studied in these works.

**Table 3** - Estimated Henry's law constants  $H_{H_2}$  for  $H_2$  dissolved in  $[C_2C_1Im][NTf_2]$  or  $[(mPEG_2)_2Im]I$  based on a linear fit of the  $H_2$  solubilities as a function of pressure at different temperatures calculated from MD simulations in Fig. 3. The statistical uncertainty ( $k = 1$ ) of the calculated  $H_{H_2}$  results is estimated to be 10%.

$T / K$	$H_{H_2} / MPa$	
	$[C_2C_1Im][NTf_2]$	$[(mPEG_2)_2Im]I$
298	405	-
323	343	-
353	291	1060
393	-	762

The solubility of other small gases such as  $CO_2$  was previously attempted to be correlated with different characteristics of the ILs [40]. Among these, the molar volume of the IL as well as the related available free volume in the liquid appear to be those with the strongest predicting power [69]. In order to test the validity of this hypothesis in the case of  $H_2$  solubility, the free volume available for accommodating  $H_2$  molecules in the IL phase was estimated by randomly generating roughly  $5 \cdot 10^5$  points in the system and computing the fraction of them that did not overlap with any atoms of the IL. Note that  $H_2$  molecules were excluded from this analysis in order to estimate the volume not occupied solely by the IL. We find that the increase of pressure leads to a slight decrease in the free volume, as can be seen in Fig. 4 for all ILs and temperatures studied. This means that  $H_2$  molecules are apparently unable to create additional volume in the system and they seem only to occupy pre-existing voids in the IL bulk. The results also show that the amount of free volume at a given pressure seems to follow the same trends observed for the  $H_2$  solubility in the two ILs at a given pressure: The higher  $T$ , the higher the amount of the free volume (in line with the increasing solubility) with the hydrophilic IL displaying less free volume (and lower solubility).

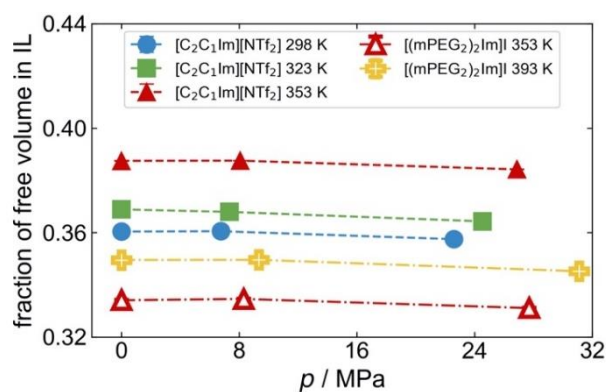


**Fig. 4** – Fraction of the free volume or voids (potentially able to host  $H_2$  molecules by solvation) in the two studied pure ILs deduced from MD simulations as a function of pressure at different temperatures. Standard errors are always smaller than the markers. Lines are only guides for the eye.

### Liquid viscosity

In Fig. 5, the SLS results for the saturated liquid viscosity  $\eta_L$  of the binary mixtures of [(mPEG<sub>2</sub>)<sub>2</sub>Im]I or [C<sub>8</sub>C<sub>1</sub>Im][PF<sub>6</sub>] with H<sub>2</sub> are presented as a function of H<sub>2</sub> pressure for two different  $T$ . The same information is also shown in Fig. 6 for mixtures of the least viscous IL [C<sub>2</sub>C<sub>1</sub>Im][NTf<sub>2</sub>] with H<sub>2</sub>, where the experimental SLS data (Fig. 6a) are compared with the simulated values (Fig. 6b) in the compressed liquid phase near saturation with dissolved H<sub>2</sub> (filled markers) or far away from saturation without H<sub>2</sub> (open markers) at three similar  $T$ . To resolve the effect of H<sub>2</sub>, the relative deviations of the viscosities of the binary IL-H<sub>2</sub> mixtures from those of the corresponding “pure” IL under a 0.1 MPa H<sub>2</sub> atmosphere are depicted in the lower parts of Figs. 5 and 6.

For the three studied IL-H<sub>2</sub> mixtures, the saturated liquid viscosities as a function of pressure up to 8 MPa agree within the combined experimental uncertainties with those for the pure ILs at 0.1 MPa. This means that dissolved H<sub>2</sub> has no significant effect on  $\eta_L$  of ILs showing a broad range of viscosity values. Comparing the three different ILs, a modest increase in viscosity with the addition of H<sub>2</sub> in the order of 5% at 8 MPa has been observed for the hydrophilic [(mPEG<sub>2</sub>)<sub>2</sub>Im]I. This behavior may be connected to the comparably lowest H<sub>2</sub> solubility among the investigated ILs, as discussed before. A somewhat more pronounced and diverging effect on the viscosity of the ILs [(mPEG<sub>2</sub>)<sub>2</sub>Im]I (+7% at 8 MPa) or [C<sub>8</sub>C<sub>1</sub>Im][PF<sub>6</sub>] (-11% at 8 MPa) was found in our previous studies [52] for the case of the weakly soluble Ar that shows yet by trend a larger solubility than H<sub>2</sub>.

Since no experimental studies on  $\eta_L$  of ILs in the presence of pressurized H<sub>2</sub> are available, the limited literature studying the effect of dissolved H<sub>2</sub> on the viscosity of organic substances can only be used for comparison. For binary mixtures of various long-chain alkanes or alcohols with H<sub>2</sub> studied at  $p$  up to 7 MPa and at  $T$  up to 573 K, the SLS experiments reported by Klein et al. [31,34] show both positive or negative deviations of  $\eta_L$  from the values of pure liquids on a small scale between (-3 to +4)%. A very similar behavior has been observed for binary mixtures of H<sub>2</sub> with methanol [35], hydrocarbon-based dehydrogenated and hydrogenated liquid organic hydrogen carriers (LOHCs) [36], and cyclic hydrocarbons such as benzene and cyclohexane [70]. Thus, the negligible changes in  $\eta_L$  induced by H<sub>2</sub> in its mixtures with non-electrolytic solvents appear to extend to mixtures with ILs.

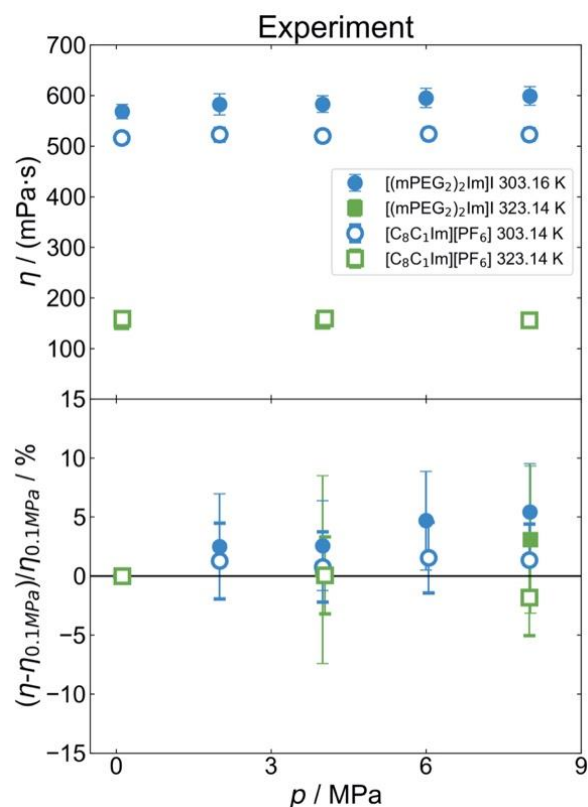


**Fig. 5** – (Top) Saturated liquid dynamic viscosity  $\eta_L$  (top) of binary mixtures of [(mPEG<sub>2</sub>)<sub>2</sub>Im]I or [C<sub>8</sub>C<sub>1</sub>Im][PF<sub>6</sub>] with dissolved H<sub>2</sub> as a function of  $p$  at (303 and 323) K obtained by SLS experiments as well as (bottom) the corresponding relative deviations of the data from the corresponding values measured at 0.1 MPa H<sub>2</sub> (solid line). (designed for single-column image)

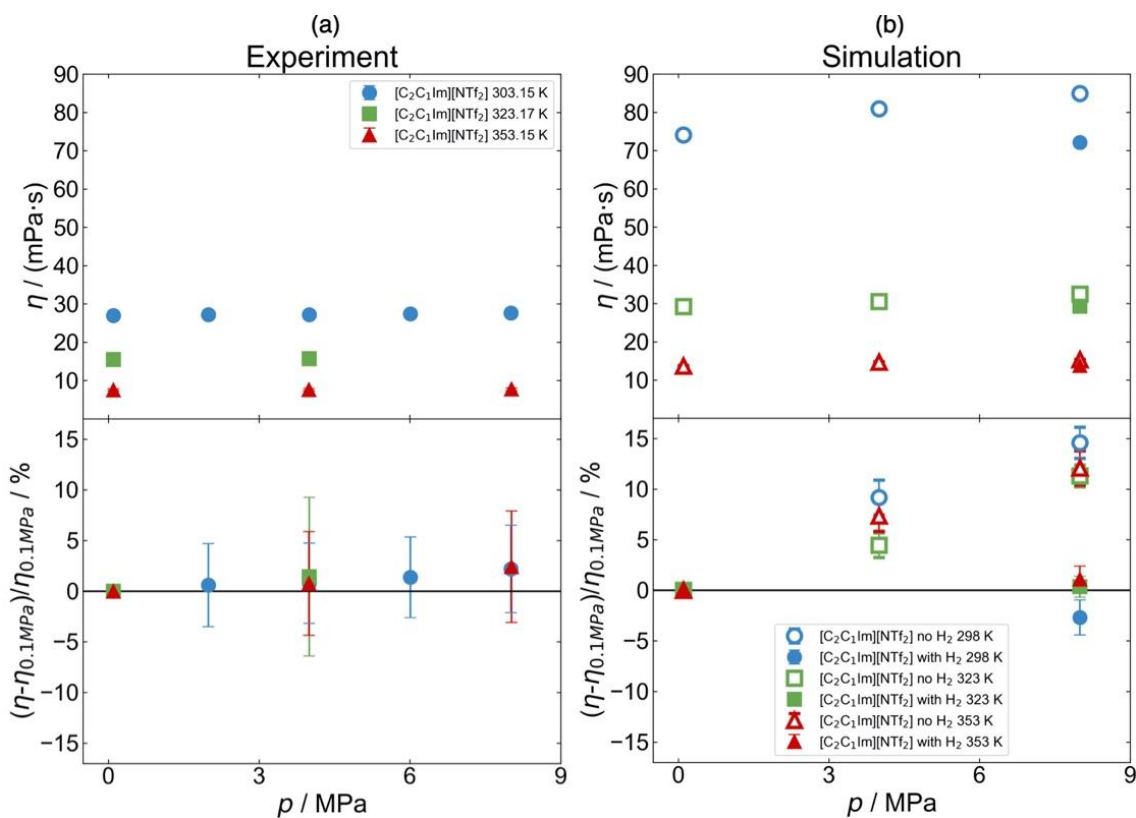


**Fig. 6** – (Top) Saturated liquid dynamic viscosity  $\eta_L$  of binary mixtures of [C<sub>2</sub>C<sub>1</sub>Im][NTf<sub>2</sub>] with dissolved H<sub>2</sub> as a function of  $p$  as well as (bottom) the relative deviations of the data from the

corresponding values obtained at 0.1 MPa H<sub>2</sub> (solid line). The experimental results for  $\eta_L$  determined by SLS at (303, 323, and 353) K in the saturated liquid phase in (a) are compared with the MD simulation results calculated in the compressed liquid phase at (298, 323, and 353) K in (b). Here, the systems with H<sub>2</sub> (empty symbols) and without H<sub>2</sub> (full markers) are dissociated. The errors bars represented the expanded uncertainties ( $k = 2$ ) of the experimental data and the statistical uncertainties ( $k = 1$ ) of the simulation results. (designed for double-column image)

In order to elucidate the origin of the viscosity behavior observed in the experiments, as mentioned before, MD simulations were performed to study  $\eta_L$  of [C<sub>2</sub>C<sub>1</sub>Im][NTf<sub>2</sub>] at  $T = (303, 323, \text{ or } 353)$  K and  $p = (0.1, 4.0, \text{ or } 8.0)$  MPa, both in the absence and in the presence of H<sub>2</sub> molecules. The former set of simulations corresponds to artificial systems, where solely the effect of  $p$  at the boundaries of the simulation cell is imitated. In the second set of simulations carried out at 8 MPa, the liquid systems contained additionally (1.96, 2.34, or 2.72) mol% H<sub>2</sub> at (303, 323, or 353) K, respectively (see Table S3 in Supporting Information), which is close to the saturation concentration of H<sub>2</sub> in the IL at equilibrium.

The comparison of the simulated and measured viscosities in Fig. 6b reveals that the simulations overestimate the viscosity by a factor of 2 to 2.5 in the studied range. While obtaining absolute viscosities with MD simulations is a major challenge, capturing relative trends can give reliable insights to the physics behind the macroscopic properties and allows to separate intertwined physical effects that would otherwise be hardly possible to be disentangled. As in our experiments, the simulated viscosities of the systems saturated with H<sub>2</sub> at 8 MPa displayed by the full symbols in Fig. 6b show basically no change with respect to the viscosity at ambient pressure irrespective of temperature. However, systems without added H<sub>2</sub> shows that the viscosity displays a strong increase with increasing  $p$ . Compared to the values at 0.1 MPa, the relative increases reach as high as (12 to 15)% at 8 MPa, as can be seen from the open symbols in Fig. 6b. This allows us to propose that the application of a H<sub>2</sub> atmosphere to ILs has two antagonizing effects. On the one hand, the increase of the pressure leads to a compression of the liquid phase, resulting in a viscosity increase of around (10 to 15)% per 10 MPa far away from the critical point. This behavior for the compressed liquid viscosity of pure fluids has been reported in the literature for ILs including those studied in this work [71–75], but also for various non-electrolytic liquids [76–78]. On the other hand, the dissolved H<sub>2</sub> has a plasticizing effect. These two effects cause a weak net increase or decrease of the viscosity and appear to be of the same relative magnitude, resulting in a constant value for  $\eta_L$  of IL-H<sub>2</sub> mixtures. We can hypothesize that the interplay of these two effects could also explain the behavior observed for other IL-gas systems such as those investigated in our former works [51,52].

## ***Interfacial properties***

### *Surface tension*

We continue with exploring the properties of the interface of the two-phase IL-H<sub>2</sub> systems as a function of pressure and temperature. Figs. 7 and 8 present the experimental (a) and simulated (b) values for the surface tension  $\sigma$  as a function of H<sub>2</sub> pressure in the top part, together with their relative deviations from the surface tensions of the pure ILs at 0.1 MPa in the bottom part. Here, Fig. 7 includes the results for the two ILs [(mPEG<sub>2</sub>)<sub>2</sub>Im]I or [C<sub>8</sub>C<sub>1</sub>Im][PF<sub>6</sub>] at two or three different  $T$ , while Fig. 8 displays the data for [C<sub>2</sub>C<sub>1</sub>Im][NTf<sub>2</sub>] at the same three  $T$  studied in the PD and SLS experiments as well as in the simulations.

The experimental data show the same trend of a slight monotonous decrease of the surface tension with increasing H<sub>2</sub> pressure. Independent of the IL and temperature, the relative decrease is within around 5% at 8 MPa compared to the reference values at 0.1 MPa. Although this decrease is weak and at the boundaries of the combined experimental uncertainties, it is consistent and resolvable throughout all data sets. This holds not only true for the PD results, but also for the SLS results for  $\sigma$  that could be determined simultaneously with the viscosity for [C<sub>2</sub>C<sub>1</sub>Im][NTf<sub>2</sub>]+H<sub>2</sub> at 353 K. Although there is a small and systematic difference of ca. 2% between the two data sets being clearly within uncertainties, the relative decrease of the surface tension determined with the PD and SLS methods is congruent. For comparison, the influence of Ar on the surface tension of the ILs [(mPEG<sub>2</sub>)<sub>2</sub>Im]I (-15% at 8 MPa) or [C<sub>8</sub>C<sub>1</sub>Im][PF<sub>6</sub>] (-19% at 8 MPa) was much more pronounced [52].

To the best of our knowledge, no measurements examining the influence of H<sub>2</sub> on the surface tension of ILs are available in the literature. At least, there are a few experimental works on the effect of H<sub>2</sub> on the surface tension of organic solvents. For different long-chain alkanes or alcohols, both positive and negative changes caused by the presence of H<sub>2</sub> within about  $\pm 5\%$  have been observed at  $p$  up 7 MPa and  $T$  up to 573 K [31,34]. The studies on methanol [35] and hydrocarbon-based LOHCs [36,79] reveal quantitatively the same H<sub>2</sub> influence on  $\sigma$  as found in the present investigation of ILs. In these studies, a linear decrease in  $\sigma$  with increasing H<sub>2</sub> pressure was found independent of  $T$ , amounting to relative changes up to -7% at 8 MPa compared to the values obtained at 0.1 MPa H<sub>2</sub>. In conclusion, the weak decrease of surface tension due to pressurized H<sub>2</sub> appears to be very similar numerically for organic solvents and ILs.

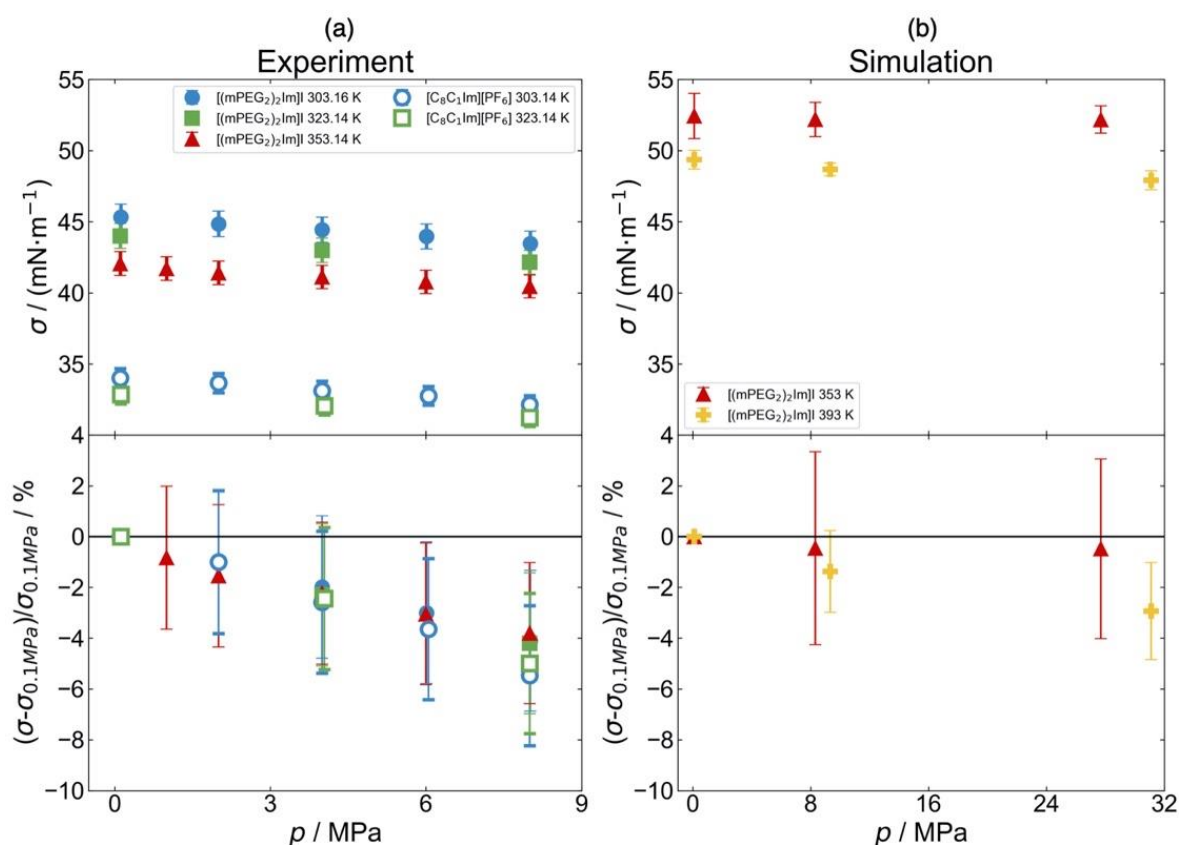


**Fig. 7** – (Top) Surface tension  $\sigma$  of binary mixtures of [(mPEG<sub>2</sub>)<sub>2</sub>Im]I or [C<sub>8</sub>C<sub>1</sub>Im][PF<sub>6</sub>] with dissolved H<sub>2</sub> as a function of  $p$  as well as (bottom) the relative deviations of the data from the corresponding values obtained at 0.1 MPa H<sub>2</sub> (solid line). The experimental results for  $\sigma$  determined by the PD method at (303, 323, and 353) K in (a) are compared with the MD simulation results for [(mPEG<sub>2</sub>)<sub>2</sub>Im]I at (353 and 393) K in (b). The errors bars represented the expanded uncertainties ( $k = 2$ ) of the experimental data and the statistical uncertainties ( $k = 1$ ) of the simulation results. (designed for double-column image)

As visible in Fig. 7b and 8b, the MD simulations yield surface tension values which are larger for the systems with [(mPEG<sub>2</sub>)<sub>2</sub>Im]I (ca. +25%) and lower for those with [C<sub>8</sub>C<sub>1</sub>Im][PF<sub>6</sub>] (ca. -11%) in comparison to the experimental data at matching  $T$ . Although the absolute values cannot be captured by the simulations since the used FFs were not calibrated against surface tension data, the relative effect of H<sub>2</sub> on  $\sigma$  is predicted very well, yet somewhat less pronounced. Furthermore, the linearly decreasing trend of  $\sigma$  as a function of  $p$  was found to continue beyond 8 MPa up to maximum pressures of 31 MPa. Within statistical uncertainties, no influence of  $T$  on the surface tension could be detected.

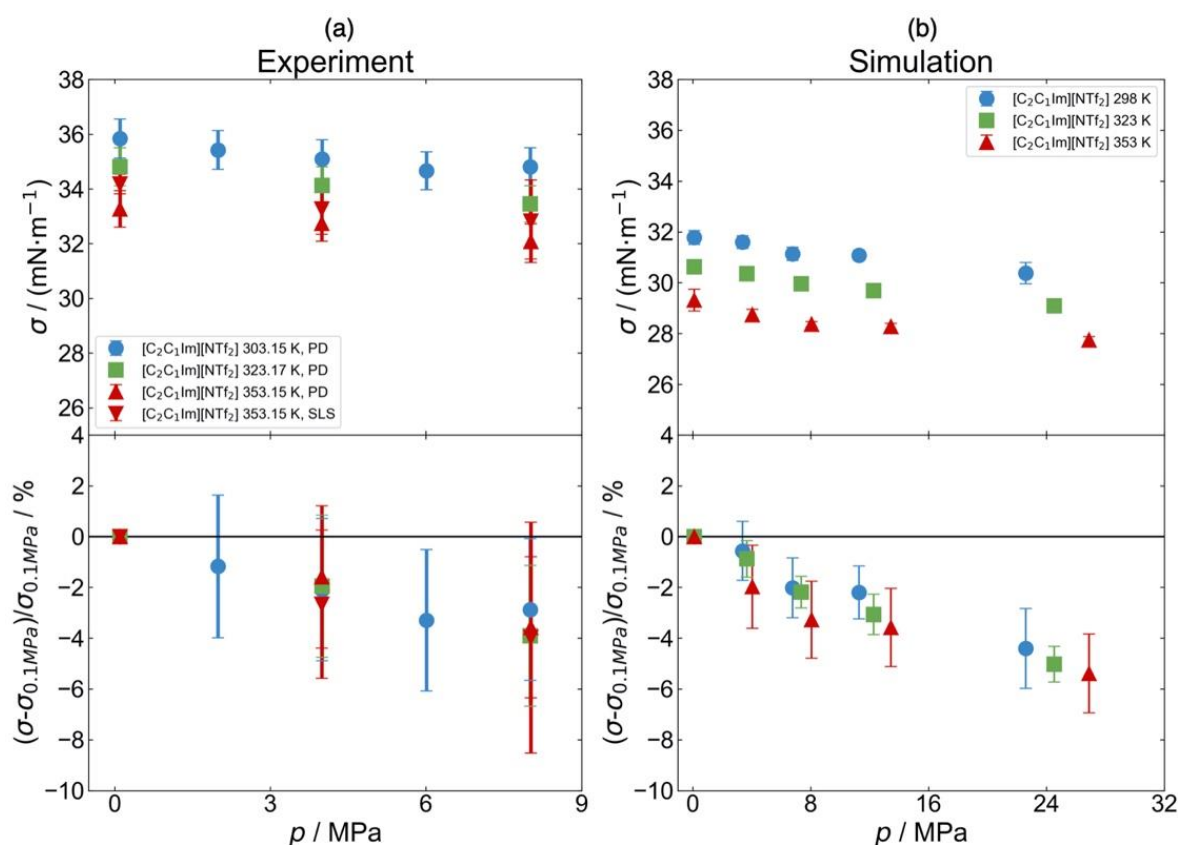


**Fig. 8** – (Top) Surface tension  $\sigma$  of binary mixtures of  $[\text{C}_2\text{C}_1\text{Im}][\text{NTf}_2]$  with dissolved  $\text{H}_2$  as a function of  $p$  as well as (bottom) the relative deviations of the data from the corresponding values obtained at 0.1 MPa  $\text{H}_2$  (solid line). The experimental results for  $\sigma$  determined by the PD method at (303, 323, and 353) K and by SLS at 353 K in (a) are compared with the MD simulation results at (298, 323, and 353) K in (b). The errors bars represented the expanded uncertainties ( $k = 2$ ) of the experimental data and the statistical uncertainties ( $k = 1$ ) of the simulation results. (designed for double-column image)

### Surface enrichment and surface structure

To elucidate the molecular-level mechanisms behind the observed reduction in surface tension with increasing  $\text{H}_2$  pressure, an in-depth investigation into the accumulation of  $\text{H}_2$  molecules at the vapor-liquid interface was undertaken. For this purpose, partial density profiles for the IL ( $\rho_{\text{IL}}$ ) and  $\text{H}_2$  ( $\rho_{\text{H}_2}$ ) were computed in  $z$ -direction across the surface of the IL slab. While the profiles for the ILs were basically insensitive to varying  $p$  and  $T$  conditions, those for  $\text{H}_2$  manifested intriguing behaviors, as illustrated in Fig. 9a with profiles computed at 298 K and four pressures from (3.4 to 22.6) MPa in  $[\text{C}_2\text{C}_1\text{Im}][\text{NTf}_2]$ . Note that in Fig. 9a, densities are plotted with respect to the average position of the interface ( $z = 0$ ). This was determined in every system from averaging the instantaneous location of the surface ions which was in turn identified with the ITIM surface analyzing technique using the pytim python library [80,81]. The partial density of  $\text{H}_2$  fluctuates around a constant value (corresponding to the given state point) in both bulk liquid and gas phases away from the surface. The partial density of  $\text{H}_2$ ,

however, goes through a maximum at the surface between its low value observed within the IL-rich phase (left side of the profiles) and the higher value computed in the gas phase containing only H<sub>2</sub> (right side of the profiles). The pressure increase leads to an increased H<sub>2</sub> density in both phases and makes the surface accumulation also more visible. The very same trend is also observed for the [(mPEG<sub>2</sub>)<sub>2</sub>Im]I+H<sub>2</sub> system as illustrated in Figure S1 in section S5 of the Supporting Information. Furthermore, the same qualitative behavior was observed for nitrogen (N<sub>2</sub>) at the surface of [C<sub>4</sub>C<sub>1</sub>Im][PF<sub>6</sub>] [48].

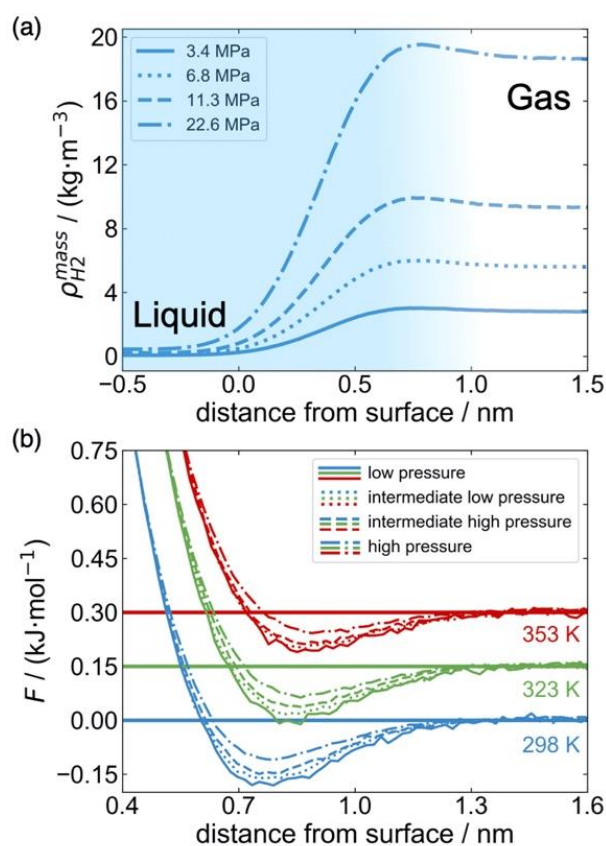


**Fig. 9** – (a) Computed partial mass density profiles of H<sub>2</sub> in the vapor-liquid system consisting of [C<sub>2</sub>C<sub>1</sub>Im][NTf<sub>2</sub>] and H<sub>2</sub> as a function of the distance from the interface computed at 298 K and different pressures as well as (b) corresponding free energy profiles of H<sub>2</sub> relative to the free energy in the H<sub>2</sub> gas phase (values of 0). In (b), the base lines of the curves computed at different temperatures are shifted by 0.15 kJ·mol<sup>-1</sup> upwards in vertical direction for clarity. The temperature-dependent low, intermediate low, intermediate high, and high pressures correspond to values in the ranges of (3.4 – 4.0) MPa, (6.8 – 8.1) MPa, (11.3 – 13.5) MPa, and (22.6 – 26.9) MPa, respectively. (designed for single-column image)

The H<sub>2</sub> density profiles normalized to their values in the gas phase can be conventionally converted to free energy ( $F$ ) profiles in order to reveal the thermodynamic forces governing the spatial distribution of H<sub>2</sub> in the system. The corresponding free energy profiles for H<sub>2</sub> dissolved in [C<sub>2</sub>C<sub>1</sub>Im][NTf<sub>2</sub>] are presented in Fig. 9b at the three studied  $T$  for the four different  $p$  values. For better visibility, the profiles computed at the different temperatures are shifted upwards by

0.15 kJ·mol<sup>-3</sup>. Fig. 8b reveals an overall very weak driving force for the H<sub>2</sub> enrichment at the surface, which is visible in the form of the minima in the free energy profiles at the same positions where  $\rho_{\text{H}_2}$  shows the maxima in Fig. 8a. The depth of the minima in Fig. 9b decrease with both increasing  $p$  and  $T$  from 0.18 kJ·mol<sup>-1</sup> at 298 K and 3.4 MPa down to 0.05 kJ·mol<sup>-1</sup> at 353 K and 26.9 MPa.

Following the approach in Ref. [82], the enrichment can be further characterized by computing the relative adsorption of H<sub>2</sub> (solute, component 2) with respect to the IL (solvent, component 1),  $\Gamma_2^{(1)}$ , which quantifies the excess number of adsorbed molecules per unit area at the interface (see equation in section S6 in the Supporting Information). The values for  $\Gamma_2^{(1)}$  obtained for [C<sub>2</sub>C<sub>1</sub>Im][NTf<sub>2</sub>] and [(mPEG<sub>2</sub>)<sub>2</sub>Im]I are listed in Table S4 in the Supporting Information and are shown in Fig. 10 as a function of  $p$  at varying  $T$ . The relatively small but positive  $\Gamma_2^{(1)}$  values confirm the previously discussed H<sub>2</sub> surface enrichment. After converting the  $\Gamma_2^{(1)}$  values shown in units of  $\mu\text{mol}/\text{m}^2$  in Fig. 10 to values in units of  $1/\text{nm}^2$ , they are by about a factor of 4 to 5 smaller than those in mixtures with solvents such as *n*-dodecane or 1-dodecanol at comparable  $p$  and  $T$  conditions [83]. Thus, surface enrichment of the non-polar H<sub>2</sub> in charged ILs systems appears to be less pronounced than in non-electrolytic organic compounds where often the non-polar alkyl segments are surface-enriched. Interestingly, for [C<sub>2</sub>C<sub>1</sub>Im][NTf<sub>2</sub>] and [(mPEG<sub>2</sub>)<sub>2</sub>Im]I studied at the same 353 K, the relative adsorption of H<sub>2</sub> is very similar although the H<sub>2</sub> solubility in the bulk IL varies by a factor of about 3.5. This similar enrichment of H<sub>2</sub> at the interface may explain the similar  $p$ -dependence of  $\sigma$  for the two ILs shown in Figs. 7 and 8. However,  $\Gamma_2^{(1)}$  at a given pressure seems to display a stronger sensitivity to temperature variation than  $\sigma$ . For the latter property, the relative percentage, but also the absolute change of the experimental surface tensions with  $p$  is very similar for different  $T$ .

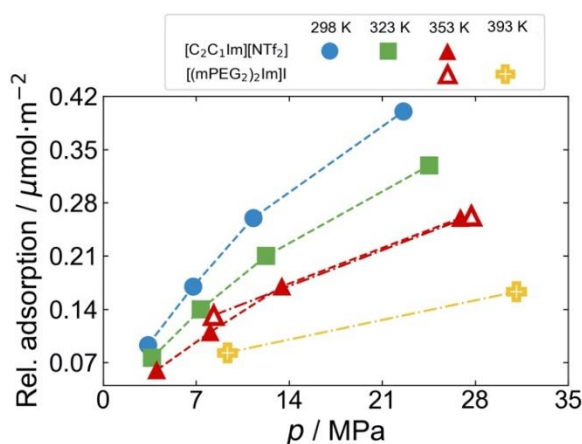


**Fig. 10** – Computed values for relative adsorption of H<sub>2</sub> at the gas-liquid interface in its mixtures with [C<sub>2</sub>C<sub>1</sub>Im][NTf<sub>2</sub>] and [(mPEG<sub>2</sub>)<sub>2</sub>Im]I as a function of pressure for different temperatures obtained from

MD simulations. The lines are fits of the data sets for the systems  $[\text{C}_2\text{C}_1\text{Im}][\text{NTf}_2]\text{-H}_2$  and serve as guides for the eye. (designed for single-column image)

Observing this subtle surface enrichment prompts the question of whether there are any structural changes induced in the organization of ions that may be linked to the accumulation of  $\text{H}_2$  at the interface. In order to shed light on this, the surface area of the ILs was calculated at selected pressures and temperatures, by disregarding  $\text{H}_2$  molecules, using the pytim python library [81]. This microscopic property was assessed using probe spheres having radii of 0.3 nm (i.e. very close to the effective size of the  $\text{H}_2$  molecules in the used FF model), 0.5 nm, 0.7 nm, and 0.9 nm, as can be seen in Fig. 11. This analysis aims to evaluate the solvent-accessible surface area (SASA), enabling the exploration of pockets or troughs of different sizes. The consequential changes in the associated surface area serve as an indicator of how roughness evolves on sub-nanometer length scales in evolving conditions.

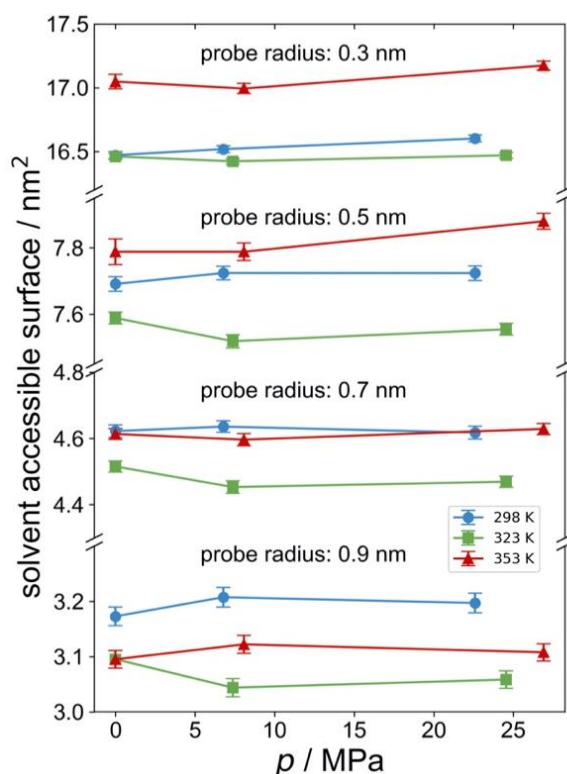


**Fig. 11** – Solvent-accessible surface area (SASA) computed by MD simulations for  $[\text{C}_2\text{C}_1\text{Im}][\text{NTf}_2]$  at different pressures and temperatures. For the analysis, different spherical probe sizes of 0.3 nm, 0.5 nm, 0.7 nm, and 0.9 nm were used. Lines are only guides for the eye.

Interestingly, the SASA values display a high insensitivity to pressure. While at 353 K, the roughness measured with the small probes shows a slight increase (no more than 2%), no clear trend is visible in other cases. That is, the nanoscopic corrugation of the surface is unaffected by the presence of  $\text{H}_2$ , as this light molecule is unable to intrude into the IL surface by creating

or enlarging adsorption pockets. This lack of change in the surface structure of ILs means that the weak decrease in the surface tension should be related to the very weak interaction energy gain due to the accumulation of H<sub>2</sub> molecules. This weak energy gain is also the driving force for the non-specific, non-invasive adsorption of H<sub>2</sub> molecules at the IL surface. It is also interesting to note that the surface roughness shows a non-trivial temperature dependence as a function of the probe size. Understanding, this interesting feature is, however, beyond the scope of the current study.

## Conclusions

The present contribution addressed the influence of H<sub>2</sub> on various bulk and interfacial properties of three selected imidazolium-based ILs at process-relevant conditions. For the first time, we reported experimental data for  $\eta_L$  and  $\sigma$  of binary mixtures of ILs with dissolved H<sub>2</sub> up to 353 K and 8 MPa by the application of SLS and PD experiments under saturation conditions. To elucidate physical origins behind the macroscopic property behavior of such highly asymmetric mixtures, we also performed MD simulations on  $\eta_L$ ,  $\sigma$ , and  $x_{H_2}$  over extended thermodynamic states up to 393 K and 31 MPa. Independent of the IL and its varying hydrophilicity, a negligible effect of H<sub>2</sub> pressure on  $\eta_L$  could be revealed experimentally and theoretically. This observation was rationalized by two counterbalancing effects, where the increase in pressure leading to a notable viscosity rise is counterbalanced by the antagonizing plasticizing influence of the H<sub>2</sub> molecules dissolved in the IL at relatively low solubilities. In the case of the gas-liquid surface tension, the experiments and simulations show a weak  $p$ -dependent decrease for all systems, amounting to about 6% reduction at 8 MPa relative to the values at 0.1 MPa based on the experiments. We could relate this decrease to a subtle surface enrichment of H<sub>2</sub>, diminishing with increasing pressure and temperature. The enrichment is accompanied by a very weak free energy change as thermodynamic driving force in the range of (0.05 to 0.2) kJ/mol. Overall, this work has shed light on the impact of H<sub>2</sub> as an energy carrier on the macroscopic and microscopic fluid behavior of ILs, which is of importance for both industry and science in the field of hydrogen technology.

## CRedit authorship contribution statement

**Ziwen Zhai:** Investigation, Methodology, Formal Analysis, Writing – Original Draft; **György Hantal:** Investigation, Methodology, Formal Analysis, Validation, Writing – Original Draft; **Arsha Cherian:** Investigation, Writing – Original Draft; **Alexander Bergen** and **Junyu Chu:**

Resources, **Christian R. Wick**: Methodology; **Karsten Meyer**: Resources, Supervision Funding acquisition; **Ana-Sunčana Smith**: Conceptualization, Validation, Writing – Review & Editing, Supervision, Project administration, Funding acquisition. **Thomas M. Koller**: Conceptualization, Validation, Writing – Review & Editing, Supervision, Project administration, Funding acquisition.

## **Funding sources**

This work was funded by the Deutsche Forschungsgemeinschaft (DFG, German Research Foundation) – Project-ID 431791331 – SFB 1452 (CLINT Catalysis at Liquid Interfaces).

## **Declaration of competing interests**

The authors declare that they have no known competing financial interests or personal relationships that could have appeared to influence the work reported in this paper.

## **Acknowledgments**

The authors gratefully acknowledge funding by the Deutsche Forschungsgemeinschaft (DFG, German Research Foundation) – Project-ID 431791331 – SFB 1452 (CLINT) and funding of the Erlangen Graduate School in Advanced Optical Technologies (SAOT) by the Bavarian State Ministry for Science and Art. A.B. is grateful for a Ph.D. fellowship provided by the Studienstiftung des deutschen Volkes.

## **Supplementary Data**

The Supporting Information of this article with supplementary information and data can be found in the online at the corresponding link. In addition, raw data related to the experiments and simulations are provided at Zenodo [84] under the following link: <https://doi.org/10.5281/zenodo.10888067>.

## References

- [1] Wasserscheid P, Welton T (eds.). *Ionic Liquids in Synthesis*. 2008 WILEY-VCH Verlag GmbH & Co. KGaA, Weinheim; 2007.
- [2] Qi H, Ren Y, Guo S, Wang Y, Li S, Hu Y et al. High-Voltage Resistant Ionic Liquids for Lithium-Ion Batteries. *ACS Appl. Mater. Interfaces* 2020;12(1):591–600. <https://doi.org/10.1021/acsami.9b16786>.
- [3] Smiglak M, Metlen A, Rogers RD. The second evolution of ionic liquids: from solvents and separations to advanced materials-Energetic examples from the ionic liquid cookbook. *Acc. Chem. Res.* 2007;40(11):1182–92. <https://doi.org/10.1021/ar7001304>.
- [4] Jiang W, Zheng D, Xun S, Qin Y, Lu Q, Zhu W et al. Polyoxometalate-based ionic liquid supported on graphite carbon induced solvent-free ultra-deep oxidative desulfurization of model fuels. *Fuel* 2017;190:1–9. <https://doi.org/10.1016/j.fuel.2016.11.024>.
- [5] Safa M, Mokhtarani B, Mortaheb HR, Tabar Heidar K, Sharifi A, Mirzaei M. Oxidative Desulfurization of Diesel Fuel Using a Brønsted Acidic Ionic Liquid Supported on Silica Gel. *Energy Fuels* 2017;31(9):10196–205. <https://doi.org/10.1021/acs.energyfuels.6b03505>.
- [6] Galiński M, Lewandowski A, Stępniaik I. Ionic liquids as electrolytes. *Electrochimica Acta* 2006;51(26):5567–80. <https://doi.org/10.1016/j.electacta.2006.03.016>.
- [7] Zhou T, Gui C, Sun L, Hu Y, Lyu H, Wang Z et al. Energy Applications of Ionic Liquids: Recent Developments and Future Prospects. *Chem. Rev.* 2023;123(21):12170–253. <https://doi.org/10.1021/acs.chemrev.3c00391>.
- [8] Jónsson E. Ionic liquids as electrolytes for energy storage applications – A modelling perspective. *Energy Storage Materials* 2020;25:827–35. <https://doi.org/10.1016/j.ensm.2019.08.030>.
- [9] Tseng H-H, Lau WJ, Al-Ghouti MA, An L (eds.). *60 Years of the Loeb-Sourirajan Membrane*. Elsevier; 2022.
- [10] Friess K, Izák P, Kárászová M, Pasichnyk M, Lanč M, Nikolaeva D et al. A Review on Ionic Liquid Gas Separation Membranes. *Membranes* 2021;11(2). <https://doi.org/10.3390/membranes11020097>.
- [11] Masataka Hatanaka, Eriko Uchiage, Mayumi Nishida, Ken-ichi Tominaga. Low-temperature Reverse Water-Gas Shift Reaction Using SILP Ru Catalysts under

- Continuous-flow Conditions. *Chemistry Letters* 2021; 50(8), 1586–1588, <https://doi.org/10.1246/cl.210184>.
- [12] Riisager A, Fehrmann R, Haumann M, Wasserscheid P. Supported Ionic Liquid Phase (SILP) Catalysis: An Innovative Concept for Homogeneous Catalysis in Continuous Fixed-Bed Reactors. *Eur. J. Inorg. Chem.* 2006;2006(4):695–706. <https://doi.org/10.1002/ejic.200500872>.
- [13] Wolf P, Wick CR, Mehler J, Blaumeiser D, Schötz S, Bauer T et al. Improving the Performance of Supported Ionic Liquid Phase Catalysts for the Ultra-Low-Temperature Water Gas Shift Reaction Using Organic Salt Additives. *ACS Catal.* 2022;12(9):5661–72. <https://doi.org/10.1021/acscatal.1c05979>.
- [14] Gu Y, Li G. Ionic Liquids-Based Catalysis with Solids: State of the Art. *Adv. Synth. Catal.* 2009;351(6):817–47. <https://doi.org/10.1002/adsc.200900043>.
- [15] Hatanaka M, Yasuda T, Uchiage E, Nishida M, Tominaga K. Continuous Gas-Phase Hydroformylation of Propene with CO<sub>2</sub> Using SILP Catalysts. *ACS Sustainable Chem. Eng.* 2021;9(35):11674–80. <https://doi.org/10.1021/acssuschemeng.1c02084>.
- [16] Rivera-Pousa A, Lois-Cuns R, Otero-Lema M, Montes-Campos H, Méndez-Morales T, Varela LM. Size Matters: A Computational Study of Hydrogen Absorption in Ionic Liquids. *J. Chem. Inf. Model.* 2024;64(1):164–77. <https://doi.org/10.1021/acs.jcim.3c01688>.
- [17] Haumann M, Jakuttis M, Werner S, Wasserscheid P. Supported ionic liquid phase (SILP) catalyzed hydroformylation of 1-butene in a gradient-free loop reactor. *Journal of Catalysis* 2009;263:321–7. <https://doi.org/10.1016/j.jcat.2009.02.024>.
- [18] Marinkovic JM, Riisager A, Franke R, Wasserscheid P, Haumann M. Fifteen Years of Supported Ionic Liquid Phase-Catalyzed Hydroformylation: Material and Process Developments. *Ind. Eng. Chem. Res.* 2019;58(7):2409–20. <https://doi.org/10.1021/acs.iecr.8b04010>.
- [19] Schörner M, Rothgängel P, Mitländer K, Wissler D, Thommes M, Haumann M. Gas-Phase Hydroformylation Using Supported Ionic Liquid Phase (SILP) Catalysts – Influence of Support Texture on Effective Kinetics. *ChemCatChem* 2021;13(19):4192–200. <https://doi.org/10.1002/cctc.202100743>.
- [20] Walter S, Haumann M, Wasserscheid P, Hahn H, Franke R. *n*-butane carbonylation to *n*-pentanal using a cascade reaction of dehydrogenation and SILP-catalyzed hydroformylation. *AIChE J.* 2015;61(3):893–7. <https://doi.org/10.1002/aic.14676>.

- [21] Desai K, Dharaskar S, Khalid M, Gedam V. Effectiveness of ionic liquids in extractive–oxidative desulfurization of liquid fuels: a review. *Chemical Papers* 2022;76(4):1989–2028. <https://doi.org/10.1007/s11696-021-02038-3>.
- [22] Wang D, Wang L, Jiao Y, Wu A, Yan H, Kang X et al. The confined growth of few-layered and ultrashort-slab Ni-promoted MoS<sub>2</sub> on reduced graphene oxide for deep-degree hydrodesulfurization. *Nano Research* 2022;15(8):7052–62. <https://doi.org/10.1007/s12274-022-4375-6>.
- [23] Wang E, Yang F, Song M, Chen G, Zhang Q, Wang F et al. Recent advances in the unsupported catalysts for the hydrodesulfurization of fuel. *Fuel Process. Technol.* 2022;235:107386. <https://doi.org/10.1016/j.fuproc.2022.107386>.
- [24] Aida Ben Hassen Trabelsi, Amina Ghrib, Kaouther Zaafour, Athar Friaa, Aymen Ouerghi, Slim Naoui et al. Hydrogen-Rich Syngas Production from Gasification and Pyrolysis of Solar Dried Sewage Sludge: Experimental and Modeling Investigations. *Biomed Res Int.* 2017; 2017: 7831470. <https://doi.org/10.1155/2017/7831470>
- [25] Kaithal A, Hölscher M, Leitner W. Carbon monoxide and hydrogen (syngas) as a C1-building block for selective catalytic methylation. *Chemical Science* 2021;12(3):976–82. <https://doi.org/10.1039/D0SC05404F>.
- [26] Khan Antara S, Hemmeter D, Zhai Z, Maier F, Koller T, Steinrück H-P et al. Hydrogenation with dissolved Pt-complexes homogenously distributed in the ionic liquid or enriched at the gas/ionic liquid interface, submitted to *ChemCatChem*, 2024.
- [27] Tavera-Méndez C-L, Bergen A, Trzeciak S, Heinemann FW, Graf R, Zahn D et al. Self-Assembled Supported Ionic Liquids. *Chem. Eur. J.* 2024;30(6):e202303673. <https://doi.org/10.1002/chem.202303673>.
- [28] Frosch M, Tavera Mendez CL, Koch AB, Schörner M, Haumann M, Hartmann M et al. Wetting Behavior and Support Interactions in Imidazolium-Based Supported Ionic Liquid Phase Materials—A Systematic Study by Solid-State Nuclear Magnetic Resonance Spectroscopy. *J. Phys. Chem. C* 2023;127(19):9196–204. <https://doi.org/10.1021/acs.jpcc.2c07795>.
- [29] Marion S, Vučemišević-Alagić N, Špadina M, Radenović A, Smith A-S. From Water Solutions to Ionic Liquids with Solid State Nanopores as a Perspective to Study Transport and Translocation Phenomena. *Small* 2021;17(25):2100777. <https://doi.org/10.1002/smll.202100777>.

- [30] Höllring K, Vučemilović-Alagić N, Smith D, Smith A-S. Criticality in an imidazolium ionic liquid fully wetting a sapphire support. 2024; <https://doi.org/10.48550/arXiv.2403.08449>.
- [31] Klein T, Lenahan FD, Zhai Z, Kerscher M, Jander JH, Koller TM et al. Viscosity and Interfacial Tension of Binary Mixtures Consisting of Linear, Branched, Cyclic, or Oxygenated Hydrocarbons with Dissolved Gases Using Surface Light Scattering and Equilibrium Molecular Dynamics Simulations. *Int J Thermophys* 2022;43(6):88. <https://doi.org/10.1007/s10765-022-03012-1>.
- [32] Andbaeva VN, Baidakov VG. Capillary constant and surface tension of propane (R-290) with small additives of hydrogen. *Fuel* 2021;287:119546. <https://doi.org/10.1016/j.fuel.2020.119546>.
- [33] Baidakov VG, Grishina KA, Khotienkova MN. Capillary constant and surface tension of ethane with small additions of hydrogen. *Fuel* 2017;207:561–7. <https://doi.org/10.1016/j.fuel.2017.06.130>.
- [34] Klein T, Lenahan FD, Kerscher M, Jander JH, Rausch MH, Koller TM et al. Viscosity and Interfacial Tension of Binary Mixtures of *n*-Hexadecane with Dissolved Gases Using Surface Light Scattering and Equilibrium Molecular Dynamics Simulations. *J. Chem. Eng. Data* 2021;66(8):3205–18. <https://doi.org/10.1021/acs.jced.1c00289>.
- [35] Kerscher M, Jander JH, Luther F, Schühle P, Richter M, Rausch MH et al. Thermophysical properties of the energy carrier methanol under the influence of dissolved hydrogen. *Int. J. Hydrogen Energy* 2023;48(69):26817–39. <https://doi.org/10.1016/j.ijhydene.2023.03.312>.
- [36] Kerscher M, Klein T, Preuster P, Wasserscheid P, Koller TM, Rausch MH et al. Influence of dissolved hydrogen on the viscosity and interfacial tension of the liquid organic hydrogen carrier system based on diphenylmethane by surface light scattering and molecular dynamics simulations. *Int. J. Hydrogen Energy* 2022;47(92):39163–78. <https://doi.org/10.1016/j.ijhydene.2022.09.078>.
- [37] Doblinger S, Silvester DS, Costa Gomes M. Functionalized Imidazolium Bis(trifluoromethylsulfonyl)imide Ionic Liquids for Gas Sensors: Solubility of H<sub>2</sub>, O<sub>2</sub> and SO<sub>2</sub>. *Fluid Phase Equilibria* 2021;549:113211. <https://doi.org/10.1016/j.fluid.2021.113211>.
- [38] Jacquemin J, Husson P, Majer V, Costa Gomes MF. Influence of the Cation on the Solubility of CO<sub>2</sub> and H<sub>2</sub> in Ionic Liquids Based on the

- Bis(trifluoromethylsulfonyl)imide Anion. *J Solution Chem* 2007;36(8):967–79.  
<https://doi.org/10.1007/s10953-007-9159-9>.
- [39] Raeissi S, Schilderman AM, Peters CJ. High pressure phase behaviour of mixtures of hydrogen and the ionic liquid family [cnmim][Tf<sub>2</sub>N]. *The Journal of Supercritical Fluids* 2013;73:126–9. <https://doi.org/10.1016/j.supflu.2012.09.003>.
- [40] Lei Z, Dai C, Chen B. Gas Solubility in Ionic Liquids. *Chem. Rev.* 2014;114(2):1289–326. <https://doi.org/10.1021/cr300497a>.
- [41] Afzal W, Liu X, Prausnitz JM. Solubilities of some gases in four imidazolium-based ionic liquids. *J. Chem. Thermodyn.* 2013;63:88.  
<https://doi.org/10.1016/j.jct.2013.03.007>.
- [42] Costa Gomes MF. Low-Pressure Solubility and Thermodynamics of Solvation of Carbon Dioxide, Ethane, and Hydrogen in 1-Hexyl-3-methylimidazolium Bis(trifluoromethylsulfonyl)amide between Temperatures of 283 K and 343 K. *J. Chem. Eng. Data* 2007;52:472. <https://doi.org/10.1021/je0604129>.
- [43] Jacquemin J, Husson P, Majer V, Padua AA, Costa Gomes MF. Thermophysical properties, low pressure solubilities and thermodynamics of solvation of carbon dioxide and hydrogen in two ionic liquids based on the alkylsulfate anion. *Green Chem.* 2008;10(9):944–50. <https://doi.org/10.1039/B802761G>.
- [44] Lynden-Bell RM. Gas-liquid interfaces of room temperature ionic liquids. *Molecular Physics* 2003;101(16):2625–33. <https://doi.org/10.1080/00268970310001592700>.
- [45] Hantal G, Voroshylova I, Cordeiro, M. Natália D. S., Jorge M. A systematic molecular simulation study of ionic liquid surfaces using intrinsic analysis methods. *Phys. Chem. Chem. Phys.* 2012;14(15):5200–13. <https://doi.org/10.1039/C2CP23967A>.
- [46] Hantal G, Sega M, Kantorovich SS, Schröder C, Jorge M. The intrinsic structure of the interface of partially miscible fluids. *J. Phys. Chem. C* 2015;119(51):28448–61.  
<https://doi.org/10.1021/acs.jpcc.5b09810>.
- [47] Seidl V, Bosch M, Paap U, Livraghi M, Zhai Z, Wick CR et al. Bis-polyethylene glycol-functionalized imidazolium ionic liquids: A multi-method approach towards bulk and surface properties. *Journal of Ionic Liquids* 2022;2(2):100041.  
<https://doi.org/10.1016/j.jil.2022.100041>.

- [48] Lapshin DN, Jorge M, Campbell EEB, Sarkisov L. On competitive gas adsorption and absorption phenomena in thin films of ionic liquids. *J. Mater. Chem. A* 2020;8(23):11781–99. <https://doi.org/10.1039/D0TA03419C>.
- [49] Kerlé D, Namayandeh Jorabchi M, Ludwig R, Wohlrab S, Paschek D. A simple guiding principle for the temperature dependence of the solubility of light gases in imidazolium-based ionic liquids derived from molecular simulations. *Phys. Chem. Chem. Phys.* 2017;19(3):1770–80. <https://doi.org/10.1039/C6CP06792A>.
- [50] Shi W, Sorescu DC, Luebke DR, Keller MJ, Wickramanayake S. Molecular Simulations and Experimental Studies of Solubility and Diffusivity for Pure and Mixed Gases of H<sub>2</sub>, CO<sub>2</sub>, and Ar Absorbed in the Ionic Liquid 1-*n*-Hexyl-3-methylimidazolium Bis(Trifluoromethylsulfonyl)amide ([hmim][Tf<sub>2</sub>N]). *J. Phys. Chem. B* 2010;114(19):6531–41. <https://doi.org/10.1021/jp101897b>.
- [51] Zhai Z, Paap U, Gezmis A, Maier F, Steinrück H-P, Koller TM. Surface tension and viscosity of binary ionic liquid mixtures from high vacuum up to pressures of 10 MPa. *J. Mol. Liq* 2023;386:122388. <https://doi.org/10.1016/j.molliq.2023.122388>.
- [52] Zhai Z, Koller TM. Influence of dissolved argon or carbon dioxide on the viscosity and surface tension of the imidazolium-based ionic liquids [OMIM][PF<sub>6</sub>] or [m(PEG<sub>2</sub>)<sub>2</sub>IM][I]. *J. Mol. Liq* 2023;377:121491. <https://doi.org/10.1016/j.molliq.2023.121491>.
- [53] Vučemilović-Alagić N, Banhatti RD, Stepić R, Wick CR, Berger D, Gaimann MU et al. Insights from molecular dynamics simulations on structural organization and diffusive dynamics of an ionic liquid at solid and vacuum interfaces. *Journal of Colloid and Interface Science* 2019;553:350–63. <https://doi.org/10.1016/j.jcis.2019.06.017>.
- [54] Zhai Z, Jander J, Bergen A, Junwei C, Meyer K, Koller TM. Combined Surface Light Scattering and Pendant-Drop Experiments for the Determination of Viscosity and Surface Tension of High-Viscosity Fluids Demonstrated for Ionic Liquids. *Int J Thermophys* 2022;43. <https://doi.org/10.1007/s10765-022-03103-z>.
- [55] Zhai Z, Koller TM. High-Temperature Measurements on Viscosity and Surface Tension of the Ionic Liquid 1-Ethyl-3-methylimidazolium Bis(trifluoromethylsulfonyl)imide ([EMIM][NTf<sub>2</sub>]) up to 473 K. *Int J Thermophys* 2023. <https://doi.org/10.1007/s10765-023-03226-x>.
- [56] Rusanov AI, Prokhorov A V. *Interfacial Tensiometry*. Amsterdam: Elsevier; 1996.
- [57] Kerscher M, Jander JH, Cui J, Martin MM, Wolf M, Preuster P et al. Viscosity, surface tension, and density of binary mixtures of the liquid organic hydrogen carrier

- diphenylmethane with benzophenone. *Int. J. Hydrogen Energy* 2022;47(35):15789–806. <https://doi.org/10.1016/j.ijhydene.2022.03.051>.
- [58] Saad SM, Neumann AW. Axisymmetric Drop Shape Analysis (ADSA): An Outline. *Adv. Colloid Interface Sci.* 2016;238:62–87. <https://doi.org/10.1016/j.cis.2016.11.001>.
- [59] Lucassen-Reynders EH, Lucassen J. Properties of capillary waves. *Adv. Colloid Interface Sci.* 1970;2(4):347–95. [https://doi.org/10.1016/0001-8686\(70\)80001-X](https://doi.org/10.1016/0001-8686(70)80001-X).
- [60] Langevin D. *Light Scattering by Liquid Surfaces and Complementary Techniques*. New York: Dekker, Marcel; 1992.
- [61] Fröba AP. Simultane Bestimmung von Viskosität und Oberflächenspannung transparenter Fluide mittels Oberflächenlichtstreuung. Dr.-Ing. thesis, Friedrich-Alexander-Universität Erlangen-Nürnberg, 2002.
- [62] Koller TM, Rausch MH, Fröba AP. Dynamic Light Scattering for the Measurement of Transport Properties of Fluids. *Int J Thermophys* 2024;45(4):57. <https://doi.org/10.1007/s10765-024-03344-0>.
- [63] Fröba AP, Will S. Light Scattering by Surface Waves - Surface Light Scattering, in: *Experimental Thermodynamics Volume IX: Advances in Transport Properties of Fluids*. Cambridge: The Royal Society of Chemistry; 2014.
- [64] Kelkar MS, Maginn EJ. Calculating the Enthalpy of Vaporization for Ionic Liquid Clusters. *J. Phys. Chem. B* 2007;111(32):9424–7. <https://doi.org/10.1021/jp073253o>.
- [65] Wang S, Hou K, Heinz H. Accurate and Compatible Force Fields for Molecular Oxygen, Nitrogen, and Hydrogen to Simulate Gases, Electrolytes, and Heterogeneous Interfaces. *J. Chem. Theory Comput.* 2021;17. <https://doi.org/10.1021/acs.jctc.0c01132>.
- [66] Baer A, Miličević Z, Smith DM, Smith A-S. Water in an electric field does not dance alone: The relation between equilibrium structure, time dependent viscosity and molecular motions. *J. Molecular Liquids* 2019; 282:303–15. <https://doi.org/10.1016/j.molliq.2019.02.055>.
- [67] Frenkel D, Smit B (eds.). *Understanding Molecular Simulation (Second Edition)*. San Diego: Academic Press; 2002.
- [68] Hess B. Determining the shear viscosity of model liquids from molecular dynamics simulations. *J. Chem. Phys.* 2002;116(1):209–17. <https://doi.org/10.1063/1.1421362>.

- [69] Shannon MS, Tedstone JM, Danielsen SPO, Hindman MS, Irvin AC, Bara JE. Free Volume as the Basis of Gas Solubility and Selectivity in Imidazolium-Based Ionic Liquids. *Ind. Eng. Chem. Res.* 2012;51(15):5565–76. <https://doi.org/10.1021/ie202916e>.
- [70] Al Harbi DK, Maddox R. Viscosity Of Hydrocarbon Liquids Saturated With Gas. Eng J Qatar University 1995.
- [71] Harris KR, Kanakubo M. Temperature and Pressure Dependence of the Viscosity of the Ionic Liquids 1-Hexyl-3-methylimidazolium Tetrafluoroborate and 1-Ethyl- and 1-Hexyl-3-methylimidazolium Bis(trifluoromethylsulfonyl)amides. *J. Chem. Eng. Data* 2021;66(12):4618–28. <https://doi.org/10.1021/acs.jced.1c00628>.
- [72] Atilhan M, Jacquemin J, Rooney D, Khraisheh M, Aparicio S. Viscous Behavior of Imidazolium-Based Ionic Liquids. *Ind. Eng. Chem. Res.* 2013;52(47):16774–85. <https://doi.org/10.1021/ie403065u>.
- [73] Ahosseini A, Scurto AM. Viscosity of Imidazolium-Based Ionic Liquids at Elevated Pressures: Cation and Anion Effects. *Int J Thermophys* 2008;29(4):1222–43. <https://doi.org/10.1007/s10765-008-0497-7>.
- [74] Harris KR, Kanakubo M, Woolf LA. Temperature and Pressure Dependence of the Viscosity of the Ionic Liquids 1-Hexyl-3-methylimidazolium Hexafluorophosphate and 1-Butyl-3-methylimidazolium Bis(trifluoromethylsulfonyl)imide. *J. Chem. Eng. Data* 2007;52(3):1080–5. <https://doi.org/10.1021/je700032n>.
- [75] Tomida D, Kumagai A, Kenmochi S, Qiao K, Yokoyama C. Viscosity of 1-Hexyl-3-methylimidazolium Hexafluorophosphate and 1-Octyl-3-methylimidazolium Hexafluorophosphate at High Pressure. *J. Chem. Eng. Data* 2007;52(2):577–9. <https://doi.org/10.1021/je060464y>.
- [76] Sanchez-Vicente Y, Emerson I, Glover R, Herbage O, Susial Martin R, Trusler JPM. Viscosities of Liquid Hexadecane at Temperatures between 323 K and 673 K and Pressures up to 4 MPa Measured Using a Dual-Capillary Viscometer. *J. Chem. Eng. Data* 2019;64(2):706–12. <https://doi.org/10.1021/acs.jced.8b00930>.
- [77] Alam MJ, Yamaguchi K, Hori Y, Kariya K, Miyara A. Measurement of thermal conductivity and viscosity of cis-1-chloro-2,3,3,3-tetrafluoropropene (R-1224yd(Z)). *International Journal of Refrigeration* 2019;104:221–8. <https://doi.org/10.1016/j.ijrefrig.2019.05.033>.

- [78] Meng XY, Sun YK, Cao FL, Wu JT, Vesovic V. Reference Correlation of the Viscosity of *n*-Hexadecane from the Triple Point to 673 K and up to 425 MPa. *J. Phys. Chem. Ref. Data* 2018;47(3):33102. <https://doi.org/10.1063/1.5039595>.
- [79] Jander JH, Schmidt PS, Giraudet C, Wasserscheid P, Rausch MH, Fröba AP. Hydrogen solubility, interfacial tension, and density of the liquid organic hydrogen carrier system diphenylmethane/dicyclohexylmethane. *Int. J. Hydrogen Energy* 2021;46(37):19446–66. <https://doi.org/10.1016/j.ijhydene.2021.03.093>.
- [80] Pártay LB, Hantal G, Jedlovszky P, Vincze A, Horvai G. A new method for determining the interfacial molecules and characterizing the surface roughness in computer simulations. Application to the liquid-vapor interface of water. *J Comput Chem* 2008;29(6):945–56. <https://doi.org/10.1002/jcc.20852>.
- [81] Segá M, Hantal G, Fábíán B, Jedlovszky P. Pytim: A python package for the interfacial analysis of molecular simulations. *J. Comput. Chem.* 2018;39(25):2118–25. <https://doi.org/10.1002/jcc.25384>.
- [82] Stephan S, Hasse H. Enrichment at vapour–liquid interfaces of mixtures: establishing a link between nanoscopic and macroscopic properties. *International Reviews in Physical Chemistry* 2020;39(3):319–49. <https://doi.org/10.1080/0144235X.2020.1777705>.
- [83] Kankanamge CJ, Lenahan FD, Klein T, Fröba AP. Viscosity and Interfacial Tension of Binary Mixtures Consisting of an *n*-Alkane, Branched Alkane, Primary Alcohol, or Branched Alcohol and a Dissolved Gas Using Equilibrium Molecular Dynamics Simulations. *Int J Thermophys* 2022;43(7):112. <https://doi.org/10.1007/s10765-022-03038-5>.
- [84] Zhai Z, Hantal G, Cherian A, Bergen A, Chu J, Wick CR et al. Influence of Molecular Hydrogen on Bulk and Interfacial Properties of Three Imidazolium-Based Ionic Liquids by Experiments and Molecular Dynamics Simulations: Zenodo; 2024. <https://doi.org/10.5281/zenodo.10888067>.